nature communications

Article

https://doi.org/10.1038/s41467-025-56879-7

8q24 derived ZNF252P promotes tumorigenesis by driving phase separation to activate c-Myc mediated feedback loop

Received: 3 June 2024

Accepted: 5 February 2025

Published online: 26 February 2025

Check for updates

Tianyu Qu[1,8], Chang Zhang[2,3,8], Xiyi Lu[1,8], Jiali Dai[1,8], Xuezhi He[4], Wei Li[1], Liang Han[5,9] ✉, Dandan Yin[6,9] ✉ & Erbao Zhang[2,7,9] ✉

As a well-known cancer risk region, the *8q24* locus is frequently amplified in a variety of solid tumors. Here we identify a pseudogene-derived oncogenic lncRNA, *ZNF252P*, which is upregulated in a variety of cancer types by copy number gain as well as *c-Myc*-mediated transcriptional activation. Mechanistically, *ZNF252P* binds and drives "phase separation" of HNRNPK and ILF3 protein in the nucleus and cytoplasm, respectively, to transcriptionally and posttranscriptionally activate *c-Myc*, thus forming a *c-Myc*/*ZNF252P*/*c-Myc* positive feedback loop. These findings expand the understanding of the relationship between genomic instability in the *8q24* region and tumorigenesis and clarify a regulatory mechanism involved in transcription and post-transcription from the perspective of RNA-mediated nuclear and cytoplasmic protein phase separation, which sheds light on the dialogue with the driver oncogene *c-Myc*. The pivotal regulatory axis of *ZNF252P*/*c-Myc* has potential as a promising biomarker and therapeutic target in cancer development.

The enabling characteristic of genome instability is a fundamental component of cancer formation and pathogenesis[1]. Copy number variation (CNV) is a type of genome instability and is closely associated with tumorigenesis. Among them, copy number amplification (CNA) is prone to involving oncogenes[2,3]. Numerous studies have focused on the role of genomic amplification-driven oncogene activation, such as the amplification of *MET*, *c-Myc* and *PIK3CA*, in various cancers[4–6]. *8q24* is the most frequently amplified region in human cancers[7,8]. Oncogenes lying within this region are often crucial regulators of tumorigenesis, such as the well-known oncogene *c-Myc*[9,10]. Therefore, focusing on the relationship between *8q24* amplification and tumorigenesis can provide a deeper understanding of the molecular mechanism underlying tumors.

As important parts of the RNA regulatory network, long noncoding RNAs (lncRNAs) play pivotal roles in tumorigenesis[11]. Our previous studies also revealed that lncRNAs can be deeply involved in oncogenesis[12–15]. Several oncogenic lncRNAs, such as *PVT1* and *FAL1*, have been found to be upregulated by copy number amplification[16,17]. The lncRNAs driven by copy number amplification in the *8q24* region still need to be further explored. Therefore, systematic and in-depth exploration of *8q24* lncRNAs in cancer is warranted.

Biomolecular condensates are composed of weak, multivalent interactions between macromolecules (such as proteins and nucleic acids)[18]. More and more evidence indicates that liquid–liquid phase separation (LLPS) is capable of reversibly and dynamically assembling macromolecular condensates[19]. Phase separation is a physiological

[1]Department of Oncology, First Affiliated Hospital of Nanjing Medical University, Nanjing, Jiangsu, PR China. [2]Department of Epidemiology, Center for Global Health, School of Public Health, Nanjing Medical University, Nanjing 211166, China. [3]The Second People's Hospital of Changzhou, the Third Affiliated Hospital of Nanjing Medical University, Nanjing, Jiangsu, PR China. [4]Department of Anatomy, Histology and Embryology, Nanjing Medical University, Nanjing, Jiangsu, PR China. [5]Department of Oncology, Xuzhou Central Hospital, Xuzhou School of Clinical Medicine of Nanjing Medical University, Xuzhou, Jiangsu, PR China. [6]Clinical Research Center, The Second Hospital of Nanjing, Nanjing University of Chinese Medicine. Zhong Fu Road, Gulou District, Nanjing, Jiangsu 210003, PR China. [7]Jiangsu Key Lab of Cancer Biomarkers, Prevention and Treatment, Collaborative Innovation Center for Cancer Personalized Medicine, Nanjing Medical University, Nanjing 211166, China. [8]These authors contributed equally: Tianyu Qu, Chang Zhang, Xiyi Lu, Jiali Dai. [9]These authors jointly supervised this work: Liang Han, Dandan Yin, Erbao Zhang. ✉e-mail: hanliang_njmu@sina.com; jsnydandan@sina.com; erbaozhang@njmu.edu.cn

process whereby a homogeneous liquid solution (or phase) composed of biomolecular components segregates into two different phases: one phase is rich in macromolecules, while the other phase is deficient in these macromolecules[20]. Biomolecular phase separation has been linked to a wide range of biological processes, including gene transcription, RNA processing, and signal transduction[21,22]. In addition, tumorigenesis is increasingly associated with abnormal phase separation[23]. Proteins containing intrinsically disordered regions (IDRs) are prone to phase separation, whereas RNA-binding proteins (RBPs) usually contain IDRs and are generally prone to multivalent interactions[24]. Interaction with RBPs is one of the important ways to realize the regulatory role of lncRNAs[25]. Moreover, RNA can trigger LLPS, this is due to its flexible structure, and has multivalent interactions[26,27]. The main molecular mechanism of RNA-driven LLPS lies in the recruitment of RNA-binding proteins (RBPs) that typically contain intrinsically disordered regions (IDRs)[28]. Currently, the involvement of RNA-driven phase separation in tumorigenesis remains poorly known, and further delineating the mechanism of this process could provide insights into the pathological mechanisms of cancer. Moreover, we know that phase separation regulation can regulate gene expression at the transcriptional or posttranscriptional level[29,30], but it is not clear that phase separation can play a regulatory role in both the nucleus and cytoplasm.

In this study, we identified a driver oncogenic lncRNA, *ZNF252P*, in the *8q24* amplification region, which is frequently upregulated in diverse cancer types and associated with poor prognosis. Copy number amplification and *c-Myc*-mediated transcriptional regulation both contribute to the elevation of *ZNF252P*. Moreover, in the nucleus, *ZNF252P* binds to HNRNPK and drives its phase separation, thereby promoting *c-Myc* transcription by binding to its promoter. In the cytoplasm, *ZNF252P* interacts with ILF3 and triggers its phase separation, thus maintaining the mRNA stability of *c-Myc*. Thus, a *ZNF252P*-mediated *c-Myc* positive feedback loop is formed, leading to continuous malignant proliferation of tumors. Together, these findings reveal that a cancer-related lncRNA functions as a crucial regulator of *c-Myc* by driving liquid droplet formation of HNRNPK and ILF3 in the nucleus and cytoplasm, suggesting its potential as a therapeutic target for cancer.

Results

8q24 region screening revealed that genomic copy number amplification drives *ZNF252P* upregulation in diverse cancer types

To systematically interrogate and screen the amplified lncRNAs in the *8q24* region, we identified 259 lncRNAs in the *8q24* region, 114 of which were expressed in the TCGA Pancancer cohort ($n = 8940$, 20 cancer types, TPM ≥ 0.1). Further analysis revealed that 22 lncRNAs were amplified in at least 25% of the samples and exhibited the correlation between the copy number amplification and expression (Supplementary Data 1). According to the average correlation coefficient across cancers, *ZNF252P* ranked first (Fig. 1A), and the top ten genes were shown in Fig. 1B. In addition to *ZNF252P*, *PVT1*, a key lncRNA that is amplified and activated in the *8q24* region, plays an important role in various types of tumorigenesis, as confirmed by numerous studies[31]. *PCAT1* and *CASC8* can also undergo copy number amplification and then be activated in esophageal and pancreatic cancer, respectively[32,33]. Since the role of *ZNF252P* in tumorigenesis remains unclear, we focused on *ZNF252P*. *ZNF252P* is located on chromosome *8q24.3* and is a pseudogene-derived lncRNA isoform. Northern blot analysis revealed that only one transcript of *ZNF252P* was determined (Supplementary Fig. 1A). Then, 5′ and 3′ rapid amplification of cDNA ends (RACE) assays identified the exact transcript length of *ZNF252P* (5454 nt, with a poly (A) tail; Supplementary Fig. 1B, C). Further observations revealed that *ZNF252P* was indeed frequently amplified across cancers (Fig. 1C). Cancer Cell Line Encyclopedia (CCLE) data also revealed that *ZNF252P* was frequently amplified in various tumor cell lines (Supplementary Fig. 1D). As shown in several common tumor types, relative to that in the copy number deletion group, the expression of *ZNF252P* was significantly elevated with copy number amplification in diverse cancer types, including non-small cell lung cancer (NSCLC), liver hepatocellular carcinoma (LIHC), colon adenocarcinoma (COAD), breast cancer (BRCA), and stomach adenocarcinoma (STAD) (Fig. 1D). The copy number was positively correlated with the expression of *ZNF252P* in these cancer types (Fig. 1E). In addition, we collected 40 NSCLC tissues to confirm that the number of *ZNF252P* copies in tumor tissues was greater than that in paired noncancerous tissues (Fig. 1F). The copy number of *ZNF252P* was positively correlated with the expression of *ZNF252P* (Fig. 1G). Consistent with the findings from the validation of the tissue samples, the lung cancer cell lines A549 and PC9 presented greater copy numbers than human bronchial epithelial (HBE) cells (Supplementary Fig. 1E).

Next, we investigated the differential expression of *ZNF252P* and found that *ZNF252P* was upregulated in NSCLC, LIHC, COAD, BRCA, and STAD in the TCGA data (Fig. 1H). Furthermore, further analysis revealed that high *ZNF252P* expression was associated with poorer overall survival (OS) in diverse cancer types (NSCLC, LIHC and BRCA), indicating its broad involvement in cancer progression (Fig. 1I). We further confirmed that *ZNF252P* was elevated in tumor tissues relative to adjacent noncancerous tissues in our own 76 paired NSCLC tissues (Fig. 1J). Further analysis revealed that advanced tumor–node–metastasis (TNM) stage was associated with increased *ZNF252P* (Fig. 1K). Higher *ZNF252P* expression predicted poorer overall survival (OS) (Fig. 1L). The above results suggest that *ZNF252P* activated by copy number amplification in the *8q24* region may play a critical role in tumorigenesis.

ZNF252P promotes cancer cell proliferation and tumorigenicity

To investigate the functional role of *ZNF252P* in cancer pathogenesis, antisense oligonucleotide (ASO)-mediated knockdown and plasmid-mediated overexpression were used to manipulate *ZNF252P* expression in multiple cancer cell lines, including A549, PC9, HepG2, HCT116, MCF7 and SGC7901 cells (Fig. 2A). MTT, colony formation and EdU assays demonstrated that inhibition of *ZNF252P* repressed the viability and proliferation capacity of diverse cancer cell lines. Conversely, overexpression of *ZNF252P* increased cell viability and proliferation (Fig. 2B–D).

To further confirm the effect of *ZNF252P* on tumorigenicity in vivo, we subcutaneously injected A549 and PC9 cells stably transfected with lentivirus-mediated sh-*ZNF252P* into nude mice. The results revealed that, compared with the control, *ZNF252P* knockdown suppressed tumor weight and volume growth. Immunohistochemical staining revealed that the expression of the proliferation marker Ki-67 was decreased in the knockdown group. In contrast, overexpression of *ZNF252P* promoted tumorigenicity in vivo, and the expression of Ki-67 was increased in the *ZNF252P*-overexpressing group (Fig. 2E). qPCR analysis was performed to examine the knockdown and overexpression efficiency of *ZNF252P* in the tumor tissues of the corresponding groups (Supplementary Fig. 2A, B).

C-Myc-mediated transcriptional activation contributes to the upregulation of *ZNF252P*

In addition to alterations at the genomic level, we further gained insights into the activation mechanisms of *ZNF252P* at the transcriptional level. By analyzing the potential transcription factor-binding sites of the *ZNF252P* promoter, we identified a *c-Myc* binding site at the promoter of *ZNF252P* (Fig. 3A). Further analysis revealed that *c-Myc* levels were correlated with *ZNF252P* in NSCLC, LIHC, COAD, BRCA and STAD samples from the TCGA cohort (Fig. 3B). These findings suggest that *c-Myc* may directly activate the transcription of *ZNF252P*. We found that *ZNF252P* expression decreased accordingly with c-Myc

https://doi.org/10.1038/s41467-025-56879-7

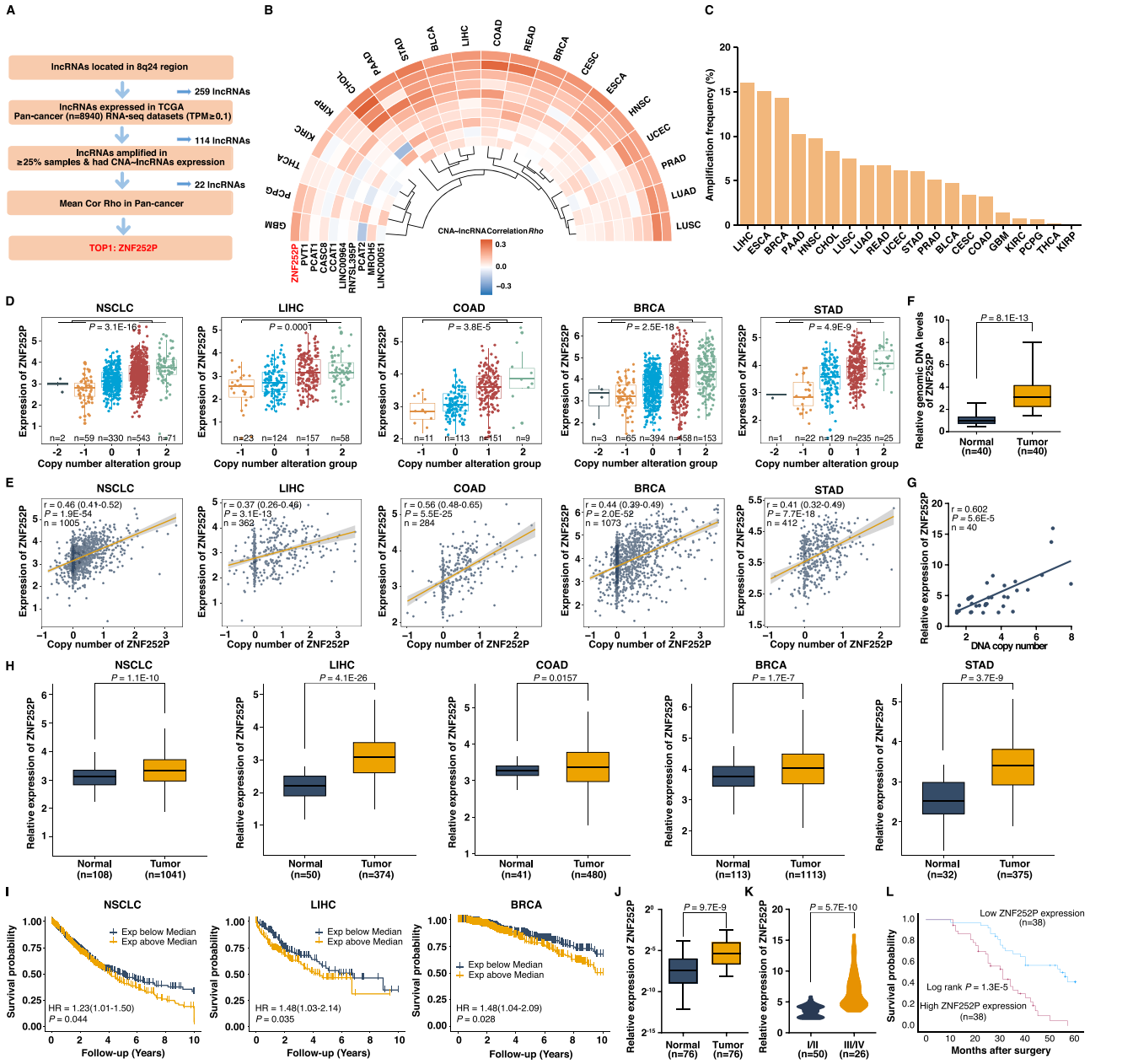

Fig. 1 | *8q24* region screening identified that genomic amplification activated-*ZNF252P* in diverse cancer types and correlates with clinicopathological characteristics. A The flow chart of lncRNA screening in *8q24* region. **B** Top 10 lncRNAs of the CNA-lncRNA in pan-cancer (order according to the average correlation coefficient). **C** Amplification frequency of *ZNF252P* in pan-cancer. **D** *ZNF252P* expression elevated with copy number amplification rather than copy number deletion in diverse cancers. Data are presented as boxplots with median (middle line), 25th, 75th percentile (box), and 5th and 95th percentile (whiskers), two-tailed Student's *t*-test. **E** The expression of *ZNF252P* was positively related to its copy number amplification (two-tailed Spearman correlation analysis). **F** The copy numbers of *ZNF252P* in tumor tissues were higher than those in paired non-cancerous tissues by qPCR analysis. Data are presented as boxplots with median (middle line), 25th, 75th percentile (box), and 5th and 95th percentile (whiskers), $n = 40$, two-tailed Student's *t*-test. **G** The copy number of *ZNF252P* was positively correlated with its expression in NSCLC tissues (two-tailed Spearman correlation analysis). **H** *ZNF252P* expression was upregulated in diverse cancers using the TCGA dataset. Data are presented as boxplots with median (middle line), 25th, 75th percentile (box), and 5th and 95th percentile (whiskers), two-tailed Student's *t*-test. **I** Higher *ZNF252P* predicted a poorer overall survival (OS) in diverse cancers. The log-rank test. **J** The *ZNF252P* expression in NSCLC tissues were higher than those in paired non-cancerous tissues by qPCR analysis. Data are presented as boxplots with median (middle line), 25th, 75th percentile (box), and 5th and 95th percentile (whiskers), $n = 76$, two-tailed Student's *t*-test. **K** Higher *ZNF252P* was related with advanced TNM stage, two-tailed Student's *t*-test. **L** Higher *ZNF252P* predicted a poorer overall survival (OS) in 76 NSCLC patients. The log-rank test. Source data are provided as a Source data file.

knockdown in A549 cells, as c-Myc overexpression had the opposite effect (Fig. 3C, D). Luciferase reporter assays revealed that *ZNF252P* promoter activity was significantly decreased when the *c-Myc* binding site was deleted compared with the full-length promoter. Moreover, overexpression of c-Myc only increased the wild-type promoter activity of *ZNF252P* without affecting the activity of the promoter of the *c-Myc* motif mutation (Fig. 3E). Furthermore, we conducted ChIP assays and confirmed that c-Myc could directly bind the *ZNF252P* promoter. The binding abundance decreased as c-Myc expression decreased and increased when c-Myc was overexpressed (Fig. 3F). Next, *ZNF252P* knockdown blunted the promoting effects of c-Myc on cell growth and colony formation (Fig. 3G and Supplementary Fig. 3A).

https://doi.org/10.1038/s41467-025-56879-7

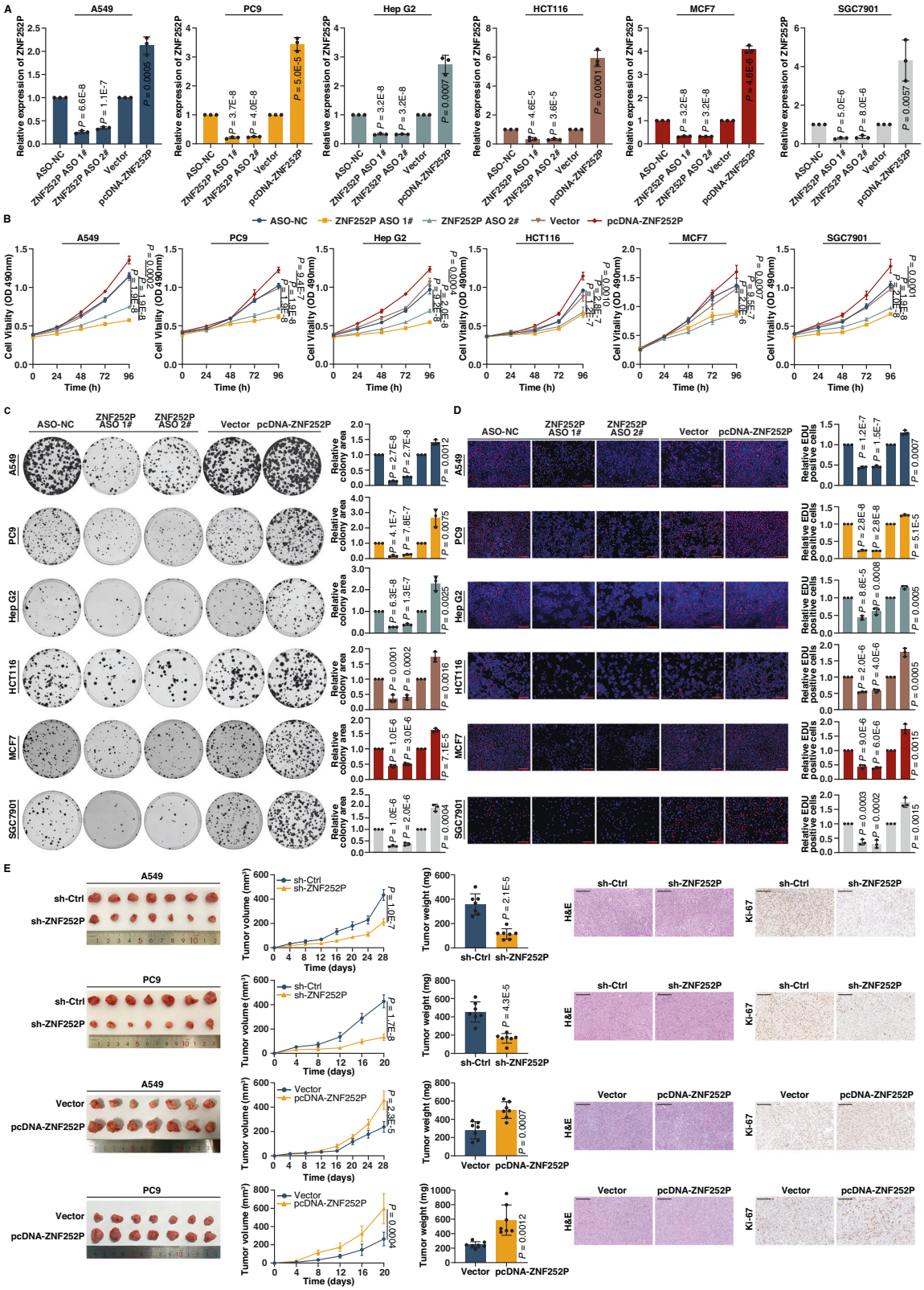

Fig. 2 | *ZNF252P* promotes cancer cell proliferation and tumorigenicity. A The efficacy of ASO-mediated knockdown and plasmid-mediated overexpression of *ZNF252P* measured by qPCR analysis. Data are mean ± s.d.; $n = 3$ independent experiments, one-way ANOVA with Dunnett's multiple comparisons test (the first three groups) or two-tailed Student's *t*-test (the last two groups). **B** The MTT, (**C**) colony formation, and (**D**) EDU assay demonstrated the effect of indicated treatments on cell proliferation. Scale bar 200 μm. Data are representatives or mean ± s.d.; $n = 3$ independent experiments, one-way ANOVA with Dunnett's multiple comparisons test (the first three groups) or two-tailed Student's *t*-test (the last two groups). **E** Stably transfected A549 and PC9 cells were injected into nude mice. Growth curves of tumor xenografts and tumor weights were measured. Representative images of tumor sections of H&E and Ki-67 IHC staining. Scale bar 200 μm. Data are representatives or mean ± s.d.; $n = 7$ mice per group, two-tailed Student's *t*-test. Source data are provided as a Source data file.

https://doi.org/10.1038/s41467-025-56879-7

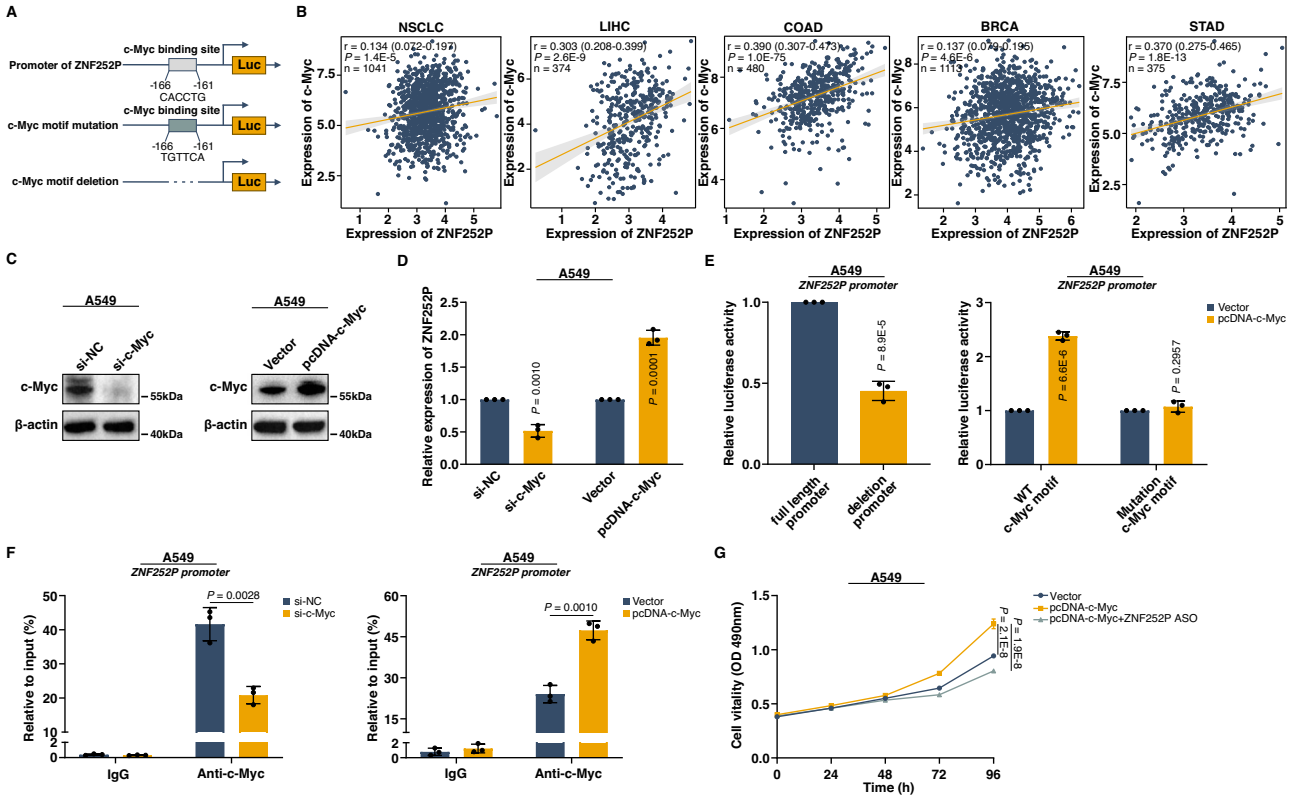

Fig. 3 | C-Myc directly transcriptionally activates *ZNF252P*. **A** Schematic diagram of *ZNF252P* promoter with the putative c-Myc binding sites and the information for mutations or deletions. **B** The expression of *ZNF252P* was positively correlated *c-Myc* expression by TCGA data in diverse cancers (two-tailed Spearman correlation analysis). **C** The immunoblotting validated the efficacy of c-Myc knockdown by siRNA and c-Myc overexpression by plasmid. Data are representatives of 3 independent experiments. **D** qPCR analysis tested *ZNF252P* expression after alteration of c-Myc. Data are mean ± s.d.; $n = 3$ independent experiments, two-tailed Student's *t*-test. **E** The dual-luciferase reporter assay determined the transcription activity of *ZNF252P* with full-length or c-Myc motif deletion promoter (left). After c-Myc overexpression, the dual-luciferase reporter assay detected the transcription capacity of *ZNF252P* with wild-type or mutated c-Myc motif in the promoter (right). Data are mean ± s.d.; $n = 3$ independent experiments, two-tailed Student's *t*-test. **F** The ChIP assay detected the enrichment of c-Myc at the *ZNF252P* promoter after alteration of c-Myc expression. Data are mean ± s.d.; $n = 3$ independent experiments, two-tailed Student's *t*-test. **G** The MTT assay demonstrated the effect of indicated treatments on cell proliferation. Data are mean ± s.d.; $n = 3$ independent experiments, one-way ANOVA with Dunnett's multiple comparisons test. Source data are provided as a Source data file.

These findings suggest that c-Myc transcriptional regulation, together with copy number amplification, is responsible for the activation of *ZNF252P*.

ZNF252P binds to HNRNPK in the nucleus and ILF3 in the cytoplasm

LncRNAs usually exert their regulatory functions by interacting with specific proteins[34]. We subsequently identified the proteins that interact with *ZNF252P* via RNA pull-down, followed by mass spectrometry (MS) analysis in A549 cells. We incubated the in vitro transcribed *ZNF252P* bound to beads with A549 cell protein extracts to purify the *ZNF252P* RNA-protein complex, and protein identity was determined by mass spectrometry (Fig. 4A). Among the highly enriched proteins (Supplementary Data 2), HNRNPK and ILF3, as RNA-binding proteins, attracted our attention because of their established oncogenic roles in tumorigenesis. *HNRNPK* is well known for its functions related to transcriptional activation regulation[35], and *ILF3* can maintain the stability of target genes at the posttranscriptional level[36]. Moreover, to further validate the physical interaction between *ZNF252P* and HNRNPK/ILF3, we performed RNA pull-down followed by Western blotting with HNRNPK/ILF3 antibodies. Our results revealed that biotin-labeled *ZNF252P* RNA, but not the empty vector or antisense *ZNF252P*, specifically retrieved HNRNPK from A549 cell nuclear protein extracts. *ZNF252P* could specifically retrieve ILF3 from A549 cell cytoplasmic protein extracts (Fig. 4A). Moreover, we found that the biotin-labeled *ZNF252P* RNA was unable to retrieve HNRNPK from A549 cell cytoplasmic protein extracts and that *ZNF252P* could not retrieve ILF3 from A549 cell nuclear protein extracts (Supplementary Fig. 4A). To further determine the specific region of *ZNF252P* that interacts with HNRNPK and ILF3, we performed deletion-mapping RNA pull-down experiments using truncated *ZNF252P*. The results revealed that the HNRNPK binding activity mapped to nucleotides 1 to 2880 of *ZNF252P* in the nuclear lysate (the main binding region is 1989-2880), whereas the ILF3 binding activity mapped to nucleotides 2881 to 5454 in the cytoplasmic lysate (the main binding region is 4590-5454) (Fig. 4B). Furthermore, we used Pprint (https://webs.iiitd.edu.in/raghava/pprint2) to analyze the potential domain in these two RBPs that is responsible for their interaction with *ZNF252P*[37]. On the basis of the prediction results, we divided the full-length HNRNPK and ILF3 into three regions: HNRNPK-R1 (1–101 amino acids), HNRNPK-R2 (102–238 amino acids), HNRNPK-R3 (239–464 amino acids), ILF3-R1 (1–262 amino acids), ILF3-R2 (263–516 amino acids), and ILF3-R3 (517–898 amino acids). We subsequently performed RIP assays using HA-tagged HNRNPK, ILF3, or their corresponding deletion mutants. In addition to confirming the binding between full-length HNRNPK and *ZNF252P* or between full-length ILF3 and *ZNF252P*, the RNA immunoprecipitation (RIP) assays also revealed that the R3 region of HNRNPK was the most important region for its binding with *ZNF252P*, and the R3 region of ILF3 was the most important region for its binding with *ZNF252P* (Fig. 4C). We further performed crosslinking immunoprecipitation

https://doi.org/10.1038/s41467-025-56879-7

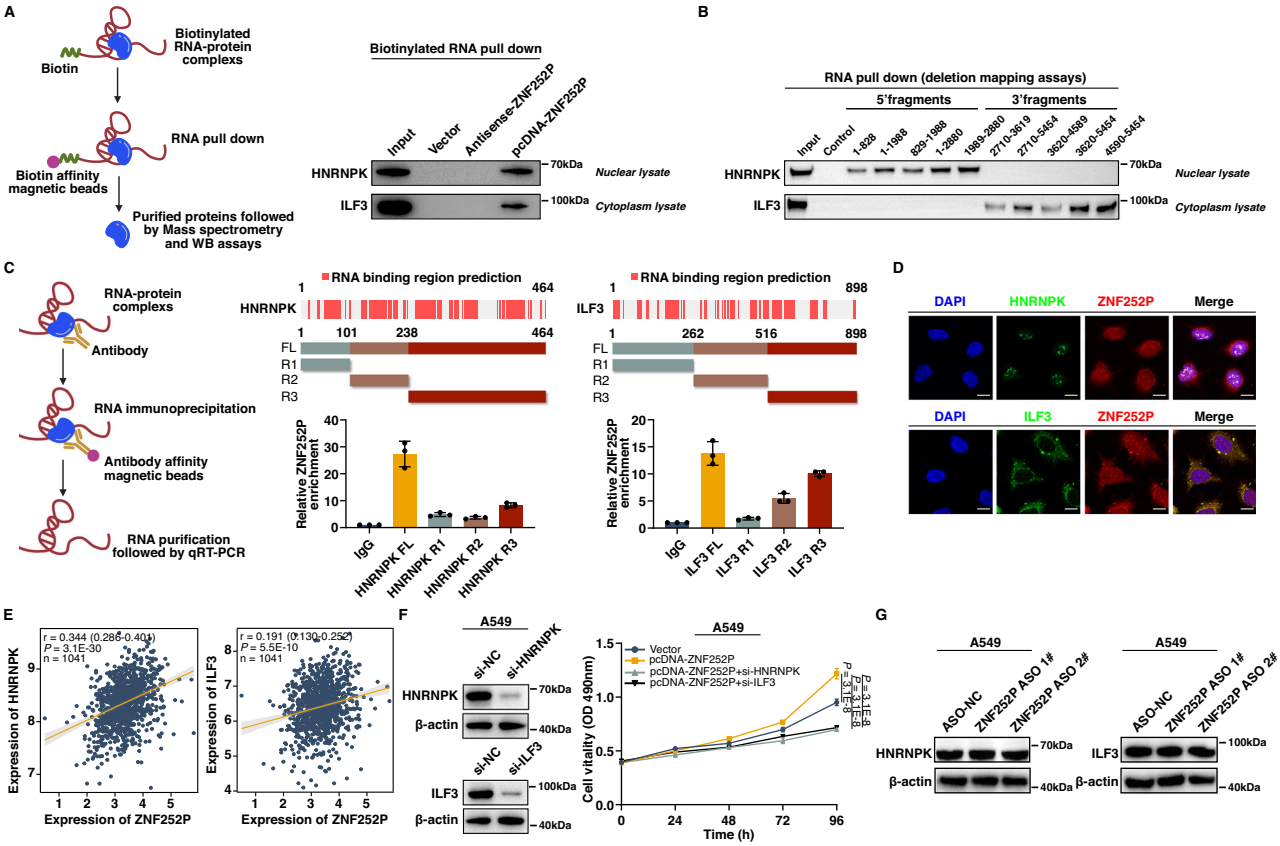

Fig. 4 | *ZNF252P* binds to HNRNPK in the nucleus and ILF3 in the cytoplasm. **A** The RNA pulldown assay followed by mass spectrometry (MS) analysis and western blot revealed the interaction between *ZNF252P*/HNRNPK and *ZNF252P*/ILF3. The samples derive from the same experiment but different gels for HNRNPK, and another for ILF3 were processed in parallel. Data are representatives of 3 independent experiments. **B** The RNA pulldown assays followed by immunoblotting were performed with a series of deletion mapping constructs of *ZNF252P*, to determine the interaction region between *ZNF252P*/HNRNPK and *ZNF252P*/ILF3. The samples derive from the same experiment but different gels for HNRNPK, and another for ILF3 were processed in parallel. Data are representatives of 3 independent experiments. **C** The RIP assays were performed using an anti-HA antibody in A549 cells transfected with HA-tagged HNRNPK or ILF3, or their deletion mutants. qPCR was used to measure the enrichment of *ZNF252P*. Data are mean ± s.d.; $n = 3$ independent experiments. **D** The co-localization analysis for *ZNF252P*/HNRNPK and *ZNF252P*/ILF3 in A549 cells. Scale bar 10μm. Data are representatives of 3 independent experiments. **E** The correlation analysis of *ZNF252P*/*HNRNPK* and *ZNF252P*/*ILF3* in TCGA NSCLC data (two-tailed Spearman correlation analysis). **F** The immunoblotting confirmed the efficacy of HNRNPK/ILF3 knockdown (left). The MTT assay showed the effect of indicated treatment on cell proliferation (right). Data are representatives or mean ± s.d.; $n = 3$ independent experiments, one-way ANOVA with Dunnett's multiple comparisons test. **G** The immunoblotting of HNRNPK or ILF3 detection after *ZNF252P* inhibition. Data are representatives of 3 independent experiments. Source data are provided as a Source data file.

(CLIP) assays followed by qPCR to further verify the interactions between *ZNF252P* and HNRNPK or ILF3. As shown in Supplementary Fig. 4B, *ZNF252P* was significantly enriched in the anti-HNRNPK immunoprecipitates or anti-ILF3 immunoprecipitates compared with the IgG control. Subsequently, RNA-protein colocalization analysis revealed that *ZNF252P* was distributed in both the nucleus and the cytoplasm, and considerable colocalization of *ZNF252P*/HNRNPK was observed in the nucleus, whereas colocalization of *ZNF252P*/ILF3 was observed in the cytoplasm (Fig. 4D). Moreover, separation of the nuclear and cytosolic fractions assay followed by qPCR also revealed that *ZNF252P* was distributed in both the nucleus and the cytoplasm (Supplementary Fig. 4C). These findings indicate that *ZNF252P* could play a regulatory role at both the transcriptional and postranscriptional levels. The TCGA data also revealed that the expression of *ZNF252P* was positively correlated with *HNRNPK* and that the expression of *ZNF252P* was positively correlated with *ILF3* (Fig. 4E). The acceleration of cell proliferation induced by *ZNF252P* was abolished after the inhibition of HNRNPK and ILF3 (Fig. 4F and Supplementary Fig. 4D). In addition, *ZNF252P* knockdown had no effect on HNRNPK or ILF3 (Fig. 4G), indicating that *ZNF252P* may promote tumorigenesis by interacting with HNRNPK/ILF3 to transcriptionally and post-transcriptionally regulate the underlying genes.

ZNF252P directly drives the phase separation of HNRNPK and ILF3 in vitro

Phase separation can regulate gene expression via the formation of biomolecular assemblies[38]. Protein sequence analysis revealed that HNRNPK and ILF3 contained amounts of IDRs[39,40] (Fig. 5A). Therefore, we speculated that *ZNF252P* may play a regulatory role both transcriptionally and posttranscriptionally by driving the LLPS of HNRNPK and ILF3. To confirm their ability to form phase separation droplets in vitro, we purified the recombinant HNRNPK and ILF3 proteins. Then, we measured the turbidity of the solution to obtain a saturation concentration of phase separation, the threshold protein concentration at which HNRNPK and ILF3 phase separation starts in buffer. The measured saturation concentration of HNRNPK is 7.23 μM, whereas that of ILF3 is 2.46 μM (Supplementary Fig. 5A). We then conducted droplet assays and observed larger and denser phase separation droplets of HNRNPK and ILF3 as the salt concentration increased (Fig. 5B). The fluorescence recovery after photobleaching (FRAP) assay demonstrated the phase separation characteristic of HNRNPK and ILF3 since the protein droplets could exchange between the puncta and the surrounding solution (Fig. 5C), suggesting their ability to undergo phase separation in vitro. We further explored the role of *ZNF252P* in the formation of phase separation droplets of HNRNPK and ILF3. First,

https://doi.org/10.1038/s41467-025-56879-7

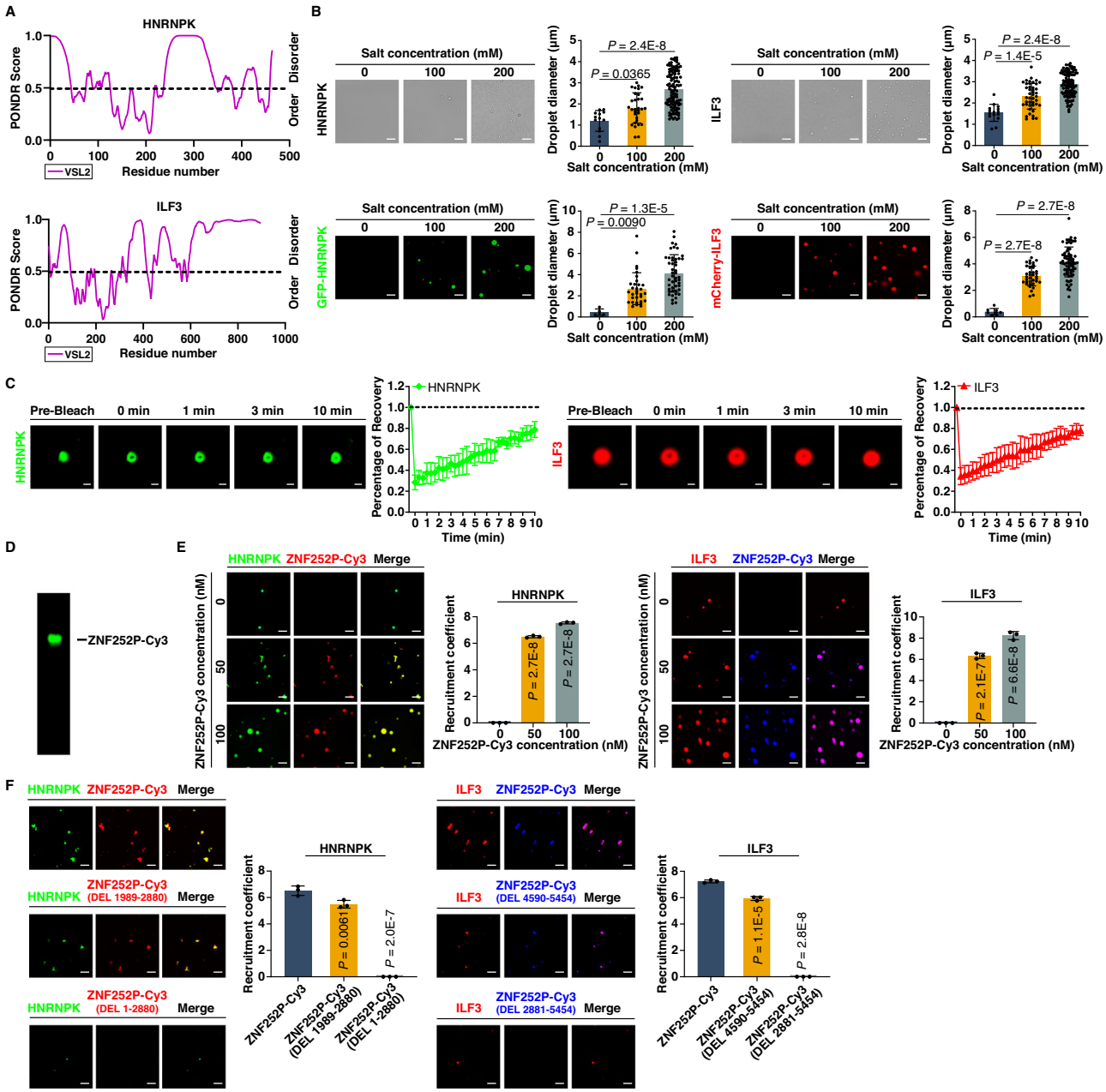

Fig. 5 | *ZNF252P* directly drives phase separation of HNRNPK and ILF3 in vitro. **A** Graph plotting intrinsically disordered regions (IDRs) of HNRNPK and ILF3 by PONDR. **B** Representative images and quantification of formed droplets of GFP-HNRNPK/mCherry-ILF3 at the indicated salt concentration in vitro. HNRNPK protein concentration: 10 μM. ILF3 protein concentration: 4 μM. Scale bar 10 μm. Data are representatives or mean ± s.d (Left panel, 0 mM: $n = 13$ droplets (HNRNPK); 100 mM: $n = 31$ droplets (HNRNPK); 200 mM: $n = 112$ droplets (HNRNPK). 0 mM: $n = 5$ droplets (GFP-HNRNPK); 100 mM: $n = 32$ droplets (GFP-HNRNPK); 200 mM: $n = 48$ droplets (GFP-HNRNPK). Right panel, 0 mM: $n = 15$ droplets (ILF3); 100 mM: $n = 43$ droplets (ILF3); 200 mM: $n = 108$ droplets (ILF3). 0 mM: $n = 8$ droplets (mCherry-ILF3); 100 mM: $n = 36$ droplets (mCherry-ILF3); 200 mM: $n = 68$ droplets (mCherry-ILF3).Three independent experiments were performed, one-way ANOVA with Dunnett's multiple comparisons test. **C** The fluorescence intensity recovery of GFP-HNRNPK and mCherry-ILF3 droplets recovered after photobleaching in vitro. Scale bar 1 μm. Data are representatives or mean ± s.d.; $n = 3$ independent experiments. **D** The fluorescent detection image of Cy3-labeled *ZNF252P*. Data are representatives of 3 independent experiments. **E** The formation and quantification of HNRNPK or ILF3 droplets in the presence of different concentrations of Cy-3 labeled *ZNF252P* RNA. Scale bar 10 μm. Data are representatives or mean ± s.d.; $n = 3$ independent experiments, one-way ANOVA with Dunnett's multiple comparisons test. **F** Representative images and quantification of the effect of *ZNF252P* deletion on HNRNPK or ILF3 droplets formation in the droplet assay. Scale bar 10 μm. Data are representatives or mean ± s.d.; $n = 3$ independent experiments, one-way ANOVA with Dunnett's multiple comparisons test. Source data are provided as a Source data file.

we obtained *ZNF252P* via in vitro transcription and labeled it with Cy3 (Fig. 5D). We found that the larger and denser droplets of *ZNF252P*/HNRNPK were augmented with increasing RNA concentrations of Cy3-*ZNF252P*. Similar results were also found in phase separation droplets of *ZNF252P*/ILF3 (Fig. 5E). These results indicate that HNRNPK can form droplets that contain *ZNF252P*, and ILF3 can form droplets that contain *ZNF252P*. We then deleted the major HNRNPK-binding region (1989-2880nt) of *ZNF252P*. We found that *ZNF252P* (DEL 1989-2880) can partially pull down HNRNPK (Supplementary Fig. 5B, upper panel) and that the droplet formation of *ZNF252P* (DEL 1989-2880)/HNRNPK was reduced compared with that of full-length *ZNF252P* (Fig. 5F, left panel). Moreover, *ZNF252P* (DEL 1-2880) could not pull down HNRNPK

(Supplementary Fig. 5B, upper panel), and the droplet formation of HNRNPK which was induced by the *ZNF252P* (DEL 1-2880) was nearly lost (Fig. 5F, left panel). In addition, deletion of the major ILF3-binding region (4590–5454 nt) of *ZNF252P* partially pulled down ILF3 (Supplementary Fig. 5B, lower panel), and the droplet formation of *ZNF252P* (DEL)/ILF3 was reduced compared with that of the full-length *ZNF252P* (Fig. 5F, right panel). Furthermore, *ZNF252P* (DEL 2881-5454) could not pull down ILF3 (Supplementary Fig. 5B, lower panel), and the droplet formation of ILF3 which was induced by the *ZNF252P* variant (DEL 2881-5454) was nearly lost (Fig. 5F, right panel). In addition, we found that the formation of discrete puncta of HNRNPK which was induced by *ZNF252P* (DEL 1989-2880) was reduced compared with that of the full-length *ZNF252P*, in the nucleus of the intact cells. The formation of discrete puncta of ILF3 which was induced by *ZNF252P* (DEL 4590-5454) was reduced compared with that of the full-length *ZNF252P*, in the cytoplasm of the intact cells (Supplementary Fig. 5C).

Compared with the *ZNF252P* deletion variant, the full-length *ZNF252P* has greater functionality in promoting phase separation of the proteins. This is highly likely because the full-length RNA sequences possess a complete structure, and the RNA structure determines the ability and behavior of RNA in the composition of the droplets[41,42].

ZNF252P drives the phase separation of HNRNPK and ILF3 in cells, thus playing a regulatory role at the transcriptional and posttranscriptional levels

Next, we explored whether HNRNPK and ILF3 can undergo phase separation in cells, which is controlled by *ZNF252P*. We separately overexpressed GFP-HNRNPK and mCherry-ILF3 in A549 cells and extracted the purified protein. Consistent with the in vitro observations, *ZNF252P* knockdown disrupted HNRNPK droplets, whereas *ZNF252P* overexpression had the opposite effect; however, *ZNF252P* antisense did not promote the formation of droplets. Similar results were also found for the phase separation of ILF3 after manipulation of *ZNF252P* expression (Fig. 6A). We further evaluated whether *ZNF252P*/HNRNPK and *ZNF252P*/ILF3 underwent phase separation in intact cells. We then observed the discrete puncta formed by HNRNPK in the nucleus and ILF3 in the cytoplasm, and HNRNPK or ILF3 fused into larger puncta after overexpression of *ZNF252P*, whereas *ZNF252P* antisense did not promote this formation (Fig. 6B). Moreover, we found that discrete puncta formed via codeposition of *ZNF252P*/HNRNPK in the nucleus and *ZNF252P*/ILF3 in the cytoplasm (Supplementary Fig. 6A). Moreover, we observed fast recovery of the fluorescence signal after bleaching via FRAP assays in cells (Fig. 6C). In addition, FRAP assays demonstrated that cell-purified HNRNPK protein or ILF3 protein was dynamic with the exchange of molecules between liquid droplets and the surrounding solution, and inhibition of *ZNF252P* decreased the speed of fluorescence signal recovery (Fig. 6D).

To explore the contribution and necessity of the IDR in phase separation droplets formation, we generated three HNRNPK-expressing constructs and ILF3-expressing constructs, including HNRNPK-IDR (247-438aa), HNRNPK with IDR deletion (HNRNPK-IDR^{DEL}), HNRNPK mutant with IDR amino acid mutation (HNRNPK-IDR^{MUT}), ILF3-IDR (342-898aa), ILF3-IDR^{DEL}, and ILF3-IDR^{MUT} (Fig. 6E). As shown in Fig. 6F, HNRNPK-IDR or ILF3-IDR formed a similar number of droplets to that of full-length HNRNPK or ILF3, whereas IDR^{DEL} or IDR^{MUT} of HNRNPK and ILF3 displayed a significantly reduced capacity. HNRNPK-IDR or ILF3-IDR formed more and larger puncta than did the corresponding IDR^{DEL} or IDR^{MUT} in intact cells (Fig. 6G). Further FRAP assays revealed rapid recovery of HNRNPK-IDR or ILF3-IDR fluorescence signals after bleaching in intact cells (Fig. 6H). HNRNPK-IDR or ILF3-IDR exchange between the droplets and the surrounding solution was also confirmed by FRAP (Fig. 6I). Together, our findings revealed that *ZNF252P* could directly promote the phase separation of HNRNPK and ILF3 in cells, thus playing a regulatory role at the transcriptional and posttranscriptional levels in tumorigenesis.

ZNF252P/HNRNPK/ILF3 promotes tumorigenesis by affecting *c-Myc*

To identify the key downstream genes of *ZNF252P*, we performed RNA sequencing after *ZNF252P* was knocked down in A549 cells (Fig. 7A, Supplementary Data 3). Gene Ontology (GO) analysis revealed that the most significantly overrepresented biological processes were involved in cell proliferation and apoptosis (Fig. 7B). Several representative tumorigenesis-related genes were validated by qPCR (Fig. 7C). Further gene set enrichment analysis (GSEA) revealed that *ZNF252P*-associated genes were involved primarily in the *c-Myc* signaling pathway (Fig. 7D). Importantly, the driver oncogene *c-Myc*, which was included in the RNA-seq data, was downregulated after *ZNF252P* was knocked down (Fig. 7C). In addition to the above positive correlation between *ZNF252P* and *c-Myc*, the correlations between *HNRNPK* and *c-Myc* and between *ILF3* and *c-Myc* were also positive in the TCGA (Fig. 7E). Therefore, we speculated that *ZNF252P* may directly regulate *c-Myc* by binding to HNRNPK and ILF3. For further confirmation, we demonstrated that the inhibition of HNRNPK or ILF3 could decrease the expression of *c-Myc* (Fig. 7F). *ZNF252P*-induced *c-Myc* expression was diminished upon inhibition of HNRNPK or ILF3 (Fig. 7G). Moreover, Western blot assays verified that the knockdown of *ZNF252P*/HNRNPK/ILF3 decreased c-Myc protein expression and that the inhibition of HNRNPK or ILF3 reversed the c-Myc expression induced by *ZNF252P* overexpression (Fig. 7H). Moreover, the overexpression of HNRNPK or ILF3 increased the protein expression of c-Myc (Supplementary Fig. 6B). In addition, the overexpression of HNRNPK or ILF3 rescued c-Myc protein expression, which was decreased by *ZNF252P* knockdown (Supplementary Fig. 6C).

As a driver oncogene, the *MYC/MAX/MAD* network is a critical pathway for *c-Myc* function[43]. Thus, we examined whether *ZNF252P* affects the *MYC/MAX/MAD* pathway by regulating *c-Myc* expression, thus promoting tumorigenesis. *MXD4* is a member of the *MYC/MAX/MAD* complex of basic transcription factors. *MXD4* can antagonize *MYC*-mediated transcriptional activation and tumorigenicity. We observed that MXD4 was elevated with *ZNF252P* knockdown and that MXD4 was decreased with *ZNF252P* overexpression. Since *MLXIPL* is a component of the antagonist of *MAD*, we found that MLXIPL expression was inhibited as *ZNF252P* was knocked down and that *ZNF252P* overexpression had the opposite effect (Fig. 7I). *MYCL* is a member of the *MYC* proto-oncogene family. We found that MYCL expression was repressed as *ZNF252P* was knocked down and that overexpression of *ZNF252P* could induce its expression (Fig. 7I). Furthermore, we found that *ZNF252P*-induced acceleration of cell proliferation could be reversed by the knockdown of c-Myc (Fig. 7J). The xenograft model further confirmed that tumor growth was increased after *ZNF252P* overexpression, whereas growth could be reversed by c-Myc knockdown. The increased Ki-67 and c-Myc expression induced by *ZNF252P* abated along with c-Myc inhibition, as shown by immunohistochemical staining (Fig. 7K). In addition, MTT assays and a xenograft model revealed that the overexpression of HNRNPK, ILF3 or c-Myc reversed the inhibitory effect of *ZNF252P* knockdown on cell proliferation both in vitro and in vivo (Fig. 7L, M).

ZNF252P activates *c-Myc* at the transcriptional and posttranscriptional levels by directly promoting the phase separation of HNRNPK and ILF3, thus forming positive *c-Myc* feedback and facilitating tumorigenesis

As HNRNPK is known for its role in transcriptional activation and *ZNF252P*-HNRNPK colocalization was observed in the nucleus, we subsequently examined the promoter transcriptional activity of *c-Myc*. As shown in Supplementary Fig. 6D, potential HNRNPK motif was located at the promoter of *c-Myc*. After knockdown of *ZNF252P*,

https://doi.org/10.1038/s41467-025-56879-7

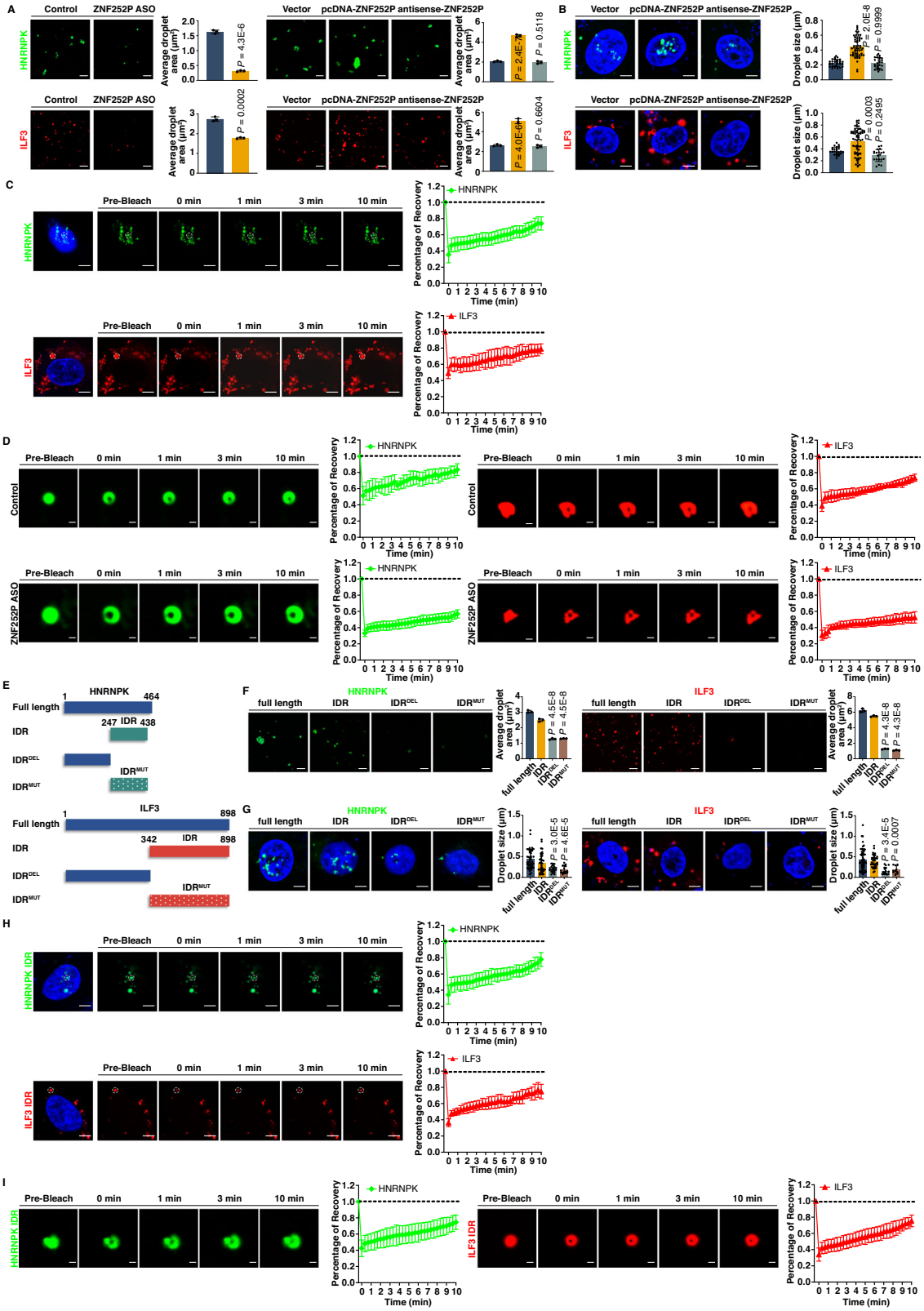

luciferase reporter assays revealed that the activity of the wild-type promoter of *c-Myc* was reduced. *ZNF252P* inhibition had no effect on the activity of HNRNPK motif-mutated (MUT) or HNRNPK motif-deleted (DEL) promoters of *c-Myc* (Fig. 8A). Moreover, ChIP assays demonstrated that HNRNPK could directly bind the *c-Myc* promoter and that the enrichment of HNRNPK in the promoter of *c-Myc* decreased after *ZNF252P* knockdown (Fig. 8B).

Importantly, we next examined whether the ability of *ZNF252P*/HNRNPK to undergo LLPS is required for the transcriptional activity of *c-Myc*. After performing dCas9-SunTag-sgRNA-mediated in situ labeling[44], we observed that endogenous HNRNPK formed droplets at the *c-Myc* promoter in cells and that overexpression of *ZNF252P* could enhance the formation of droplets (Fig. 8C). Furthermore, we constructed a *c-Myc* promoter DNA probe, and in vitro droplets assays

Fig. 6 | *ZNF252P* drives phase separation of HNRNPK and ILF3 in the nucleus and cytoplasm of cells, respectively. A Representative images and quantification of cell-purified HNRNPK or ILF3 droplets formation after manipulation of *ZNF252P*. Scale bar 10μm. Data are representatives or mean ± s.d.; $n = 3$ independent experiments, two-tailed Student's *t*-test (left panel) or one-way ANOVA with Dunnett's multiple comparisons test (right panel). **B** HNRNPK or ILF3 formed discrete puncta in A549 cells. Scale bar 5μm. Data are representatives or mean ± s.d (Upper panel, Vector: $n = 30$ droplets (HNRNPK); pcDNA-*ZNF252P*: $n = 54$ droplets (HNRNPK); antisense-*ZNF252P*: $n = 26$ droplets (HNRNPK). Lower panel, Vector: $n = 26$ droplets (ILF3); pcDNA-*ZNF252P*: $n = 64$ droplets (ILF3); antisense-*ZNF252P*: $n = 20$ droplets (ILF3). Three independent experiments were performed, one-way ANOVA with Dunnett's multiple comparisons test. **C** The fluorescence intensity of HNRNPK or ILF3 droplets recovered after bleaching in the intact A549 cells. Scale bar 5μm. Data are representatives or mean ± s.d.; $n = 3$ independent experiments. **D** Knockdown of *ZNF252P* repressed recovery capacity of HNRNPK or ILF3. Scale bar 1μm. Data are representatives or mean ± s.d.; $n = 3$ independent experiments. **E** Schematic illustration of HNRNPK or ILF3. **F** The droplets formation of HNRNPK or ILF3 and their mutants. Scale bar 10 μm. Data are representatives or mean ± s.d.; $n = 3$ independent experiments, one-way ANOVA with Dunnett's multiple comparisons test. **G** The droplet puncta in intact A549 cells transfected with HNRNPK or ILF3 and their mutants. Scale bar 5 μm. Data are representatives or mean ± s.d (Left panel, full length: $n = 49$ droplets (HNRNPK); IDR: $n = 37$ droplets (HNRNPK); IDR^{DEL}: $n = 21$ droplets (HNRNPK); IDR^{MUT}: $n = 16$ droplets (HNRNPK). Right panel, full length: $n = 54$ droplets (ILF3); IDR: $n = 38$ droplets (ILF3); IDR^{DEL}: $n = 14$ droplets (ILF3); IDR^{MUT}: $n = 12$ droplets (ILF3)). Three independent experiments were performed, one-way ANOVA with Dunnett's multiple comparisons test. **H** The fluorescence intensity of HNRNPK-IDR or ILF3-IDR droplets recovered after bleaching in A549 cells. Scale bar 5μm. Data are representatives or mean ± s.d.; $n = 3$ independent experiments. **I** The fluorescence intensity of HNRNPK-IDR or ILF3-IDR droplets. Scale bar 1μm. Data are representatives or mean ± s.d.; $n = 3$ independent experiments. Source data are provided as a Source data file.

revealed that, compared with WT droplets, droplets formed by HNRNPK showed significantly recruitment decline of the MUT DNA probes derived from the *c-Myc* promoter. The overexpression of *ZNF252P* increased the droplets formed by HNRNPK via the recruitment of DNA probes derived from the *c-Myc* promoter; nevertheless, the antisense *ZNF252P* did not have this effect (Fig. 8D). Next, we examined the necessity of the HNRNPK IDR for *c-Myc* transcriptional activation. Through the luciferase reporter assays, we found that full-length HNRNPK and HNRNPK-IDR increased the transcriptional activity of *c-Myc*, whereas HNRNPK-IDR^{DEL} or HNRNPK-IDR^{MUT} had no effect on *c-Myc* transcriptional activity (Fig. 8E, left panel). Further assays revealed that *ZNF252P* knockdown decreased the ability of full-length HNRNPK or HNRNPK-IDR to promote *c-Myc* promoter activity (Fig. 8E, right panel). qPCR revealed that HNRNPK or HNRNPK-IDR promoted the expression of *c-Myc*, whereas HNRNPK-IDR^{DEL} or HNRNPK-IDR^{MUT} had no effect on *c-Myc* expression (Fig. 8F). Taken together, at the transcriptional level, these findings indicate that *ZNF252P* promotes *c-Myc* transcription by driving HNRNPK phase separation.

To further confirm the relationship between *ZNF252P*/ILF3/c-Myc, colocalization analysis revealed that *ZNF252P*/ILF3/c-Myc colocalized in the cytoplasm (Fig. 8G). Furthermore, we performed the RIP assay and found that knockdown of *ZNF252P* weakened the interaction between ILF3 and *c-Myc* mRNA, indicating that *ZNF252P* can regulate the interaction between ILF3 and *c-Myc* and is necessary for the expression of *c-Myc* (Fig. 8H). Next, we divided *c-Myc* mRNA into three fragments: the 5′ untranslated region (5′-UTR), coding sequence (CDS), and 3′-UTR. The subsequent RNA pull-down assays revealed that only the 3′-UTR of *c-Myc*, not the 5′-UTR or CDS, could retrieve ILF3 (Fig. 8I).

Since ILF3 is known for its role in maintaining mRNA stability, we aimed to determine whether *ZNF252P* regulates *c-Myc* mRNA stability via ILF3. A luciferase reporter assay revealed that inhibition of ILF3 did not affect the transcriptional activity of the *c-Myc* promoter (Fig. 8J), which further indicated that ILF3 affected *c-Myc* expression after transcription. We then treated A549 cells with actinomycin D to prevent mRNA synthesis and measured the remaining *c-Myc* mRNA within a fixed interval. We found that knockdown of *ZNF252P* or ILF3 reduced the half-life of *c-Myc* (Fig. 8K). We further confirmed that *ZNF252P*/ILF3 regulates *c-Myc* in a phase-separated manner. By laser confocal analysis, we observed denser and larger droplet formation when ILF3 was incubated with the *c-Myc* 3′-UTR, but droplets were rarely found with the *c-Myc* 5′-UTR (Fig. 8L, left). The puncta formation capability was further strengthened by the mixture of the ILF3/*c-Myc* 3′-UTR and *ZNF252P*, but not the *ZNF252P* antisense (Fig. 8L, right), indicating the vital role of *ZNF252P* in mediating phase separation between ILF3 and *c-Myc*. We subsequently examined the necessity of the ILF3 IDR for *c-Myc* posttranscriptional stability. As shown in Fig. 8M (left panel), the *c-Myc* mRNA in cells transfected with ILF3 or ILF3 IDR had an extended half-life, whereas no effect was found in the ILF3-IDR^{DEL} or ILF3-IDR^{MUT} group. Further assays revealed that *ZNF252P* knockdown decreased the stabilizing effect of full-length ILF3 or ILF3-IDR on *c-Myc* mRNA (Fig. 8M, right panel). qPCR revealed that ILF3 or ILF3-IDR could indeed induce *c-Myc* expression, but ILF3-IDR^{DEL} or ILF3-IDR^{MUT} had no effect on *c-Myc* expression (Fig. 8N). Taken together, these findings indicate that at the posttranscriptional level, *ZNF252P* promotes *c-Myc* by driving ILF3 phase separation.

Importantly, not only did the transcript activity of the *ZNF252P* promoter increase after the overexpression of c-Myc (Fig. 3E), but the *ZNF252P* promoter activity was also increased by the overexpression of *ZNF252P* itself (Fig. 8O). Similarly, *ZNF252P* promoter activity was also increased by the overexpression of HNRNPK or ILF3 (Fig. 8O). Therefore, we concluded that c-Myc and *ZNF252P* constitute a positive feedback regulatory loop that promotes tumorigenesis.

To further confirm the relationship between *ZNF252P* and c-Myc, we used the small-molecule c-Myc inhibitor 10058-F4 and found that it attenuated c-Myc expression in a dose-dependent manner (Fig. 9A). The viability of the cells treated with 10058-F4 was attenuated, and the combination of the *ZNF252P* inhibitor and 10058-F4 further augmented this repression (Fig. 9B, C). To explore the therapeutic potential of *ZNF252P* in vivo, since antisense oligonucleotides (ASOs) have promising therapeutic potential in vivo[45], we used an in vivo-optimized ASO for *ZNF252P*. In the cell xenograft model, the combination of 10058-F4 and ZNF2525P ASO showed a greater effect on tumor inhibition in vivo, and IHC staining of the xenografts revealed that both c-Myc and Ki-67 decreased after the inhibition of *ZNF252P* and c-Myc (Fig. 9D). qPCR analysis was performed to examine *ZNF252P* levels in the tumor tissues (Supplementary Fig. 6E). In addition, patient-derived xenograft (PDX) models are generated by directly implanting tumor tissues from patients with tumors into immunodeficient mice. PDX models are considered a priority option for evaluating personalized treatments[46]. Thus, we developed patient-derived xenograft (PDX) models with two lung cancer patients (PDX 1# and PDX 2#). As shown in Fig. 9E, when the tumor xenografts were palpable, and intratumoral administration of the in vivo-optimized *ZNF252P* ASO repressed tumor growth. In addition, 10058-F4, a small-molecule inhibitor of c-Myc, can also inhibit tumor growth. Importantly, the combination of *ZNF252P* inhibitor and c-Myc inhibitor showed better inhibitory effect, indicating the therapeutic potential of *ZNF252P*/*c-Myc* in tumorigenesis. IHC staining of PDXs revealed that c-Myc and Ki-67 both decreased after the inhibition of *ZNF252P*, and c-Myc. qPCR was used to detect *ZNF252P* levels in the tumor tissues of the corresponding groups of PDXs (Supplementary Fig. 6F).

Discussion

Genomic instability is an important genetic feature of malignant tumors. As a recognized cancer risk region, a wide range of solid tumors are often amplified at the *8q24* locus[47–49], which is one of the

https://doi.org/10.1038/s41467-025-56879-7

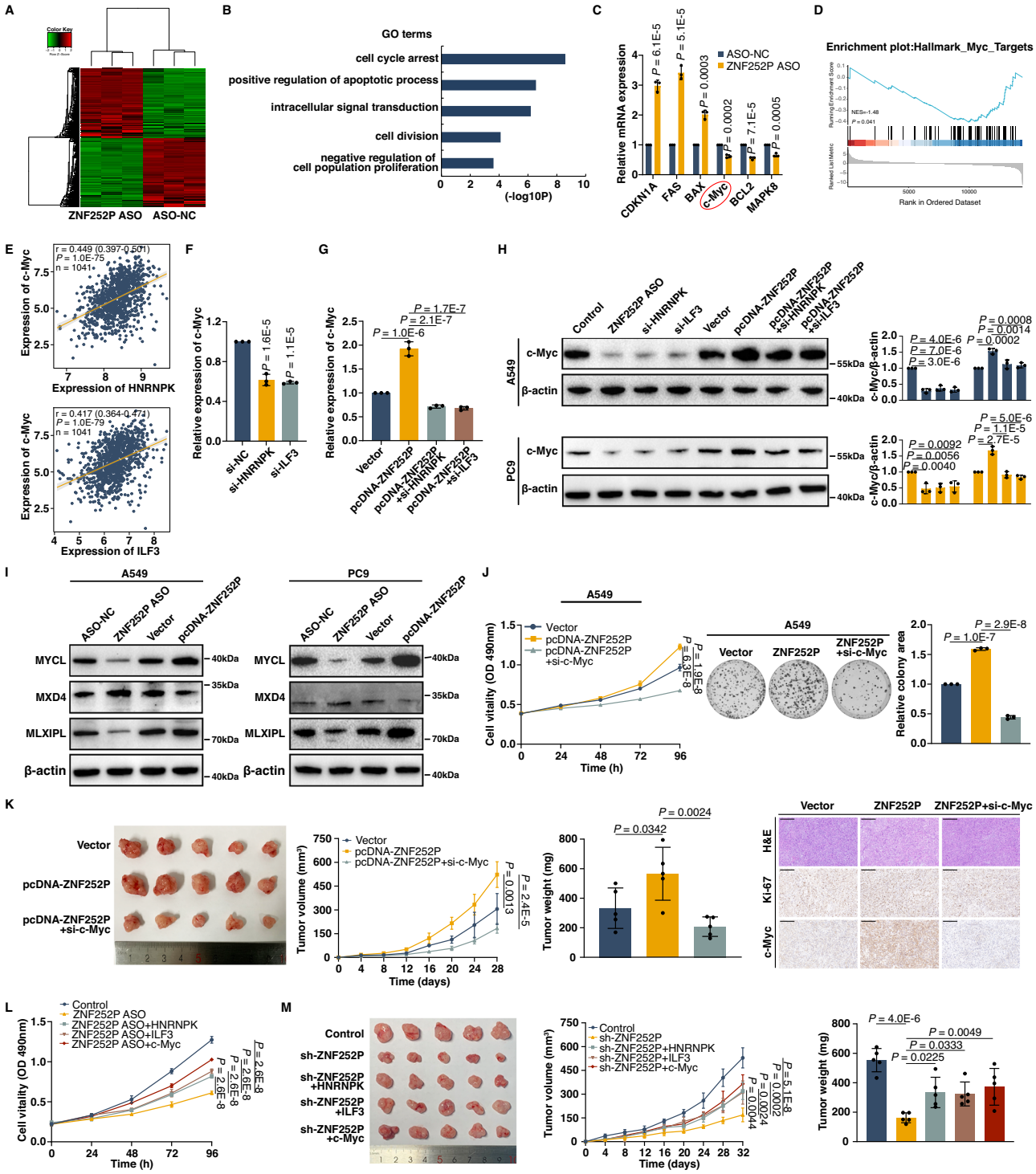

crucial genomic factors leading to tumorigenesis[50]. Several genes located at *8q24* that are frequently amplified in various cancer types, such as the driver oncogene *c-Myc*, are known to drive cancer pathogenesis[7]. Amplification of lncRNAs, such as *PVT1*, has also been observed at *8q24* in human cancers[47]. We identified an oncogenic driver RNA, *ZNF252P*, at *8q24*, which is driven by copy number amplification. *ZNF252P* is upregulated in diverse cancer types and promotes cancer cell proliferation and tumorigenicity. Our findings expand the network between genomic instability at *8q24* and tumorigenesis. In addition, we also found that c-Myc-mediated transcriptional activation at the transcriptional level contributed to the upregulation of *ZNF252P*. As an important oncogenic transcription factor, *c-Myc* has also been demonstrated to facilitate cancer development and progression[51]. *C-Myc* could recognize and bind to the E-box DNA elements. We also investigated the effects of several E-box-related transcription factors, including USF1, USF2, TFEB, and TWIST1. We found that the knockdown of USF1, USF2, TFEB, and TWIST1 has no significant impact on the expression of *ZNF252P* (data not shown), indicating the exclusive importance of *c-Myc* in this cascade. We identified the transcriptional activation of *ZNF252P* as a mechanism involved in *c-Myc* carcinogenicity, indicating that *ZNF252P* may represent a potential target for counteracting the oncogenic axis of *c-Myc* signaling.

Growing evidence shows that abnormal phase segregation is considered an important mechanism of gene regulation and can be

Fig. 7 | *ZNF252P*/HNRNPK/ILF3 promotes tumorigenesis by affecting *c-Myc*. **A** RNA sequencing was performed after inhibition of *ZNF252P*. **B** GO analysis for differentially expressed genes after inhibition of *ZNF252P*. **C** qPCR assay was performed to verify the results of RNA-seq. Data are mean ± s.d.; $n = 3$ independent experiments, two-tailed Student's *t*-test. **D** GSEA analysis showed the gene sets were enriched in c-Myc targets. **E** The correlation between *HNRNPK* or *ILF3* and *c-Myc*. (two-tailed Spearman correlation analysis). **F** qPCR analysis of *c-Myc* expression after inhibition of HNRNPK or ILF3. Data are mean ± s.d.; $n = 3$ independent experiments, one-way ANOVA with Dunnett's multiple comparisons test. **G** qPCR analysis of *c-Myc* expression after indicted treatments. Data are mean ± s.d.; $n = 3$ independent experiments, one-way ANOVA with Dunnett's multiple comparisons test. **H** Representative images and quantification of immunoblotting assays of c-Myc expression after indicated treatments. Data are representatives or mean ± s.d.; $n = 3$ independent experiments, one-way ANOVA with Dunnett's multiple comparisons test. **I** The protein expression changes of MYC pathway-related genes after alteration of *ZNF252P*. Data are representatives of 3 independent experiments. **J** The MTT and colony formation assay demonstrated the effect of indicated treatments on cell proliferation. Data are representatives or mean ± s.d.; $n = 3$ independent experiments, one-way ANOVA with Dunnett's multiple comparisons test. **K** The transfected A549 cells were injected into nude mice. Growth curves of tumor xenografts and tumor weights were measured. Representative images of tumor sections of H&E and IHC staining (Ki-67 and c-Myc) were shown. Scale bar 200 μm. Data are representatives or mean ± s.d.; $n = 5$ mice per group, one-way ANOVA with Dunnett's multiple comparisons test. **L** The MTT assay demonstrated the effect of indicated treatments on cell proliferation. Data are mean ± s.d.; $n = 3$ independent experiments, one-way ANOVA with Dunnett's multiple comparisons test. **M** The transfected A549 cells were injected into nude mice. Growth curves of tumor xenografts and weight in nude mice with indicated treatments. Data are representatives or mean ± s.d.; $n = 5$ mice per group, one-way ANOVA with Dunnett's multiple comparisons test. Source data are provided as a Source data file.

involved in disease processes, including tumorigenesis[23]. Recent studies have shown that RBPs often contain an abundance of IDR regions, indicating their high potential for phase separation[28]. Our previous studies demonstrated that the RBPs IGF2BP1 and YBX1 can undergo phase separation to promote tumorigenesis[12,15]. In our present study, HNRNPK and ILF3, as RBPs, both undergo phase separation. In addition to proteins, RNA can also make important contributions to biomolecular phase separation. For example, the lncRNA *SNHG9* can drive the phase separation of LATS1 to promote oncogenic YAP signaling[52]. The glutamine starvation-induced lncRNA *GIRGL* drives the phase separation of CAPRIN1 to restrain *GLS1* expression during oncogenesis[53]. Therefore, the mechanisms underlying RNA-mediated RBP phase separation in tumorigenesis warrant further elucidation. In addition to the above advances, the subcellular localization of biomolecular phase separation is crucial for their regulatory role. For example, at the transcriptional level, the transcriptional activator yes-associated protein (YAP) forms phase segregation droplets in the nucleus, which induces the transcription of its target genes in tumorigenesis[54,55]. At the posttranscriptional level, miRNAs associate with Argonaute2 (Ago2) proteins to form the core of the miRNA-induced silencing complex (miRISC), and the miRISC can undergo phase separation, thus post-transcriptional inhibition of target genes in the cytoplasm[30]. However, it is unclear whether phase separation regulation can be carried out in both the nucleus and cytoplasm. In our study, we revealed that the lncRNA *ZNF252P* binds and drives phase separation of HNRNPK in the nucleus and ILF3 in the cytoplasm, thus playing a regulatory role at the transcriptional and posttranscriptional levels. HNRNPK mainly activates gene expression at the transcriptional level, and ILF3 mainly maintains mRNA stability after transcription. HNRNPK is a member of the heterogeneous nuclear ribonucleoprotein (hnRNP) family, and previous reports have demonstrated that multiple hnRNPs undergo phase separation[56], such as the role of HNRNPA1 in the assembly of stress granules to promote pathological fibrillization[57]. However, the understanding of HNRNPK phase separation in pathogenesis is limited. ILF3 is activated in a variety of tumors, but its regulatory role in phase separation seems unknown. Our data suggest that *ZNF252P* can promote the phase separation of HNRNPK and ILF3. We describe RNA-mediated regulation from the perspective of nuclear phase separation and cytoplasmic phase separation. In addition, we found that full-length HNRNPK or ILF3 have more functionality than IDR mutants, do in the experiments pertaining to the exploration of the IDR function. These findings indicate that the complete protein-folding domain is important for maintaining protein phase separation and exerting its functionality.

The oncogene *c-Myc* is located at the center of human cancers. In the present study, we revealed that c-Myc and *ZNF252P* constitute a positive feedback regulatory loop that is *ZNF252P*-dependent and proceeds in a *ZNF252P*-driven phase separation mode. *ZNF252P* activates *c-Myc* at the transcriptional and posttranscriptional levels by directly promoting the phase separation of HNRNPK and ILF3. This finding partially explains the persistent activation of c-Myc in tumors. A previous study revealed that HNRNPK directly transcriptionally activates *c-Myc*[58]; however, the mechanism by which this process is regulated remains unclear. Our data revealed a mechanism by which *ZNF252P* promotes *c-Myc* transcription by binding to HNRNPK in a phase-separated manner. In addition, we discovered the direct post-transcriptional regulation of *c-Myc* by *ZNF252P*/ILF3 in a phase-separated manner. We also investigated the function of *ZNF252P*/*c-Myc* in vivo. We found that the combination of a *ZNF252P* inhibitor and a c-Myc inhibitor resulted in excellent antitumor characteristics in PDX models, indicating that *ZNF252P*/*c-Myc* could be a promising therapeutic target for cancer. Certainly, *ZNF252P* may also regulate the expression of genes other than *c-Myc*. For example, our RNA-seq data found that Yes-associated protein (YAP1) was decreased after the knockdown of *ZNF252P* (Supplementary Data 3). YAP1 is a major downstream effector of the Hippo signaling pathway, which is pervasively activated and exerts oncogenic activities in human malignancies[59,60]. Previous studies revealed that HNRNPK can directly bind the YAP1 promoter and transcriptionally activate YAP1 expression[61,62]. Therefore, *ZNF252P* may promote tumorigenesis by binding to HNRNPK and transcriptionally activating *YAP1* expression. This is a limitation of our study, and we will further investigate this aspect in our future work.

In conclusion, our results suggest that *ZNF252P* contributes to cancer development and progression driven by the genomic amplification of *8q24*. Our findings provide insights into the integration of *c-Myc* signaling in tumorigenesis, the mechanism by which phase separation driven by *ZNF252P* mediates transcriptional and post-transcriptional regulation (Fig. 9F). This study indicates that *ZNF252P*/*c-Myc* may serve as a potential anticancer target in tumorigenesis.

Methods

Study approval

This study was approved by the Ethics Committee on Human Research of the First Affiliated Hospital of Nanjing Medical University. The written informed consent was obtained from all patients. All the animal experiments were approved by the Institutional Animal Care and Use Committee (IACUC) of Nanjing Medical University.

Screening of lncRNAs driven by genomic amplification in the *8q24* region across cancers

The lncRNA profiles in the *8q24* region were obtained via cytoband annotation from the GENCODE project (hg19 genome build, https://www.gencodegenes.org/). Then, we extracted corresponding lncRNA expression and copy number variation (CNV) level data from The Cancer Genome Atlas (TCGA) project. Gene-level RNA-seq data (expression levels in terms of transcripts per million (TPM)), CNV data

https://doi.org/10.1038/s41467-025-56879-7

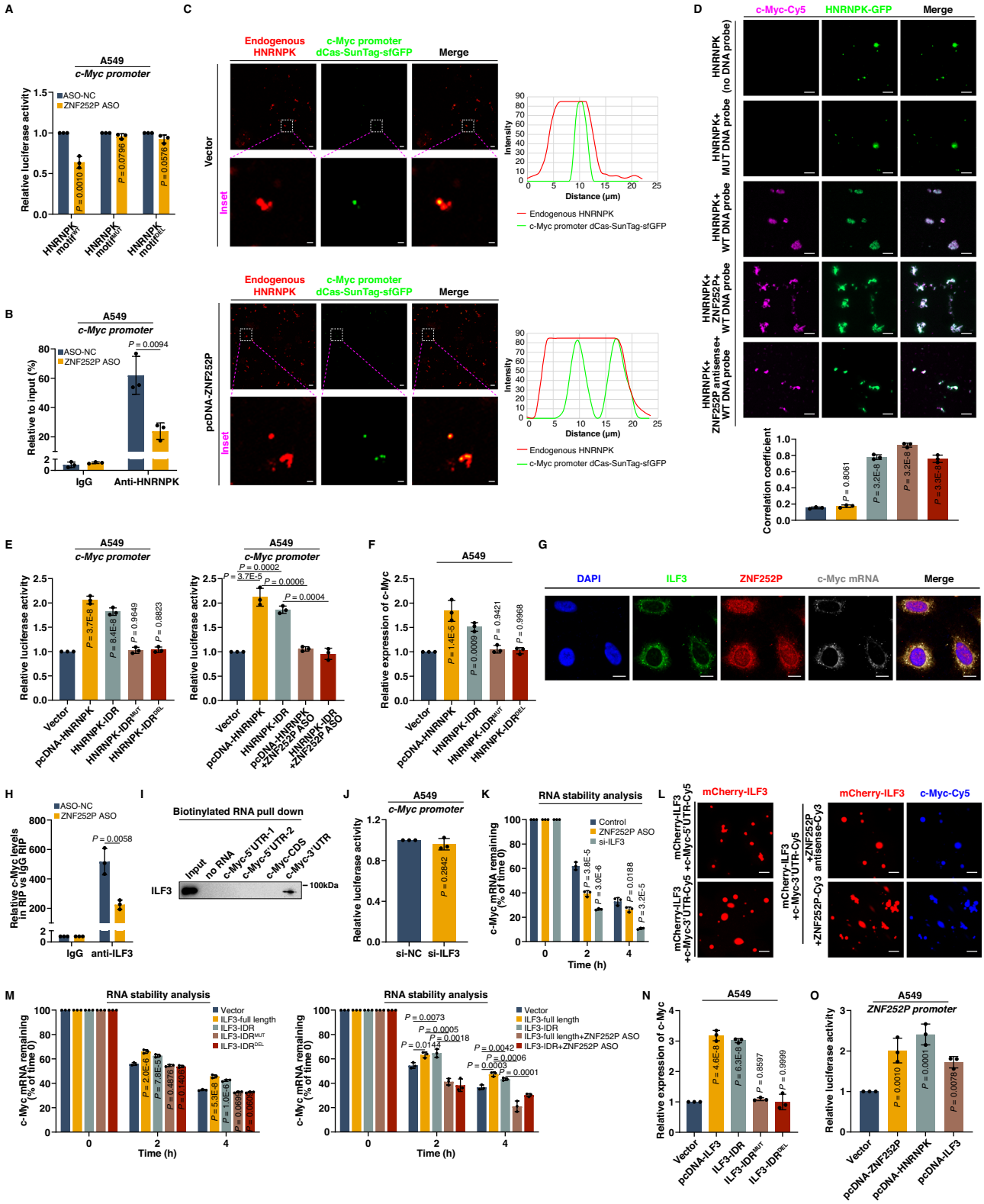

and corresponding clinical data from the TCGA project were obtained from the UCSC Xena browser (https://xena.ucsc.edu/)[63]. Twenty common cancer types in TCGA[64] were included in our analysis. The processed TCGA copy number variations were called from GISTIC2.0 software, and the thresholds were classified into -2, -1, 0, 1, and 2, which represent genes undergoing homozygous deletion, copy number loss, copy number normalization, copy number gain, and amplification, respectively. Spearman's rank correlation was used to estimate the correlation between CNV levels and gene expression. We used an integrated approach to select candidate lncRNAs across cancers, which takes both correlation strength (Rho) and the number of cancer types with correlations into consideration.

Tissue sample collection and ethics statement

We collected the paired NSCLC tissues along with adjacent non-cancerous tissues from the patients undergoing surgery at the First

Fig. 8 | *ZNF252P* activates *c-Myc* by promoting LLPS of HNRNPK and ILF3, forming c-Myc feedback loop. A Transcription activity of *c-Myc* with corresponding treatments. Data are mean ± s.d.; $n = 3$ independent experiments, two-tailed Student's *t*-test. **B** The enrichment of HNRNPK at *c-Myc* promoter after *ZNF252P* knockdown. Data are mean ± s.d.; $n = 3$ independent experiments, two-tailed Student's *t*-test. **C** Cells with positive localization of HNRNPK droplets at the sfGFP sites (c-Myc promoter). Scale bar, 5 µm (main images), 1 µm (insets). Data are representatives of 3 independent experiments. **D** The droplets formation with indicated treatments. Scale bar 10µm. Data are representatives or mean ± s.d.; $n = 3$ independent experiments, one-way ANOVA with Dunnett's multiple comparisons test. **E** *c-Myc* promoter activity with corresponding treatments. Data are mean ± s.d.; $n = 3$ independent experiments, one-way ANOVA with Dunnett's multiple comparisons test. **F** *c-Myc* expression with corresponding treatment. Data are mean ± s.d.; $n = 3$ independent experiments, one-way ANOVA with Dunnett's multiple comparisons test. **G** Colocalization assay of *ZNF252P*/ILF3/c-Myc. Scale bar 10µm. Data are representatives of 3 independent experiments. **H** The enrichment of *c-Myc* immunoprecipitated with anti-ILF3. Data are mean ± s.d.; $n = 3$ independent experiments, two-tailed Student's *t*-test. **I** The binding sites of ILF3 were mapped to 3′UTR of *c-Myc*. Data are representatives of 3 independent experiments. **J** Transcription activity of *c-Myc* after knockdown ILF3. Data are mean ± s.d.; $n = 3$ independent experiments, two-tailed Student's *t*-test. **K** Remaining c-Myc *mRNA* after actinomycin D treatment. Data are mean ± s.d.; $n = 3$ independent experiments, one-way ANOVA with Dunnett's multiple comparisons test. **L** mCherry-ILF3 was incubated with corresponding RNA. Scale bar 10 µm. Data are representatives of 3 independent experiments. **M** Remaining *c-Myc* mRNA after actinomycin D treatment. Data are mean ± s.d.; $n = 3$ independent experiments, one-way ANOVA with Dunnett's multiple comparisons test. **N** *c-Myc* expression with ILF3 and its mutants. Data are mean ± s.d.; $n = 3$ independent experiments, one-way ANOVA with Dunnett's multiple comparisons test. **O** Transcription activity of *ZNF252P* with corresponding treatments. Data are mean ± s.d.; $n = 3$ independent experiments, one-way ANOVA with Dunnett's multiple comparisons test. Source data are provided as a Source data file.

Affiliated Hospital of Nanjing Medical University. The tissues were stored in the RNA*later* solution (RNA stabilization solution, Invitrogen, Thermo), then frozen in the liquid nitrogen. The samples were kept at -80 °C until the extraction of RNA. The clinical characteristics of the patients are summarized in Supplementary Table 1.

Cell culture
The cell lines used in the study were purchased from the National Collection of Authenticated Cell Cultures, Chinese Academy of Sciences (Shanghai, China). They were cultured in RPMI 1640 or DMEM supplemented with 10% fetal bovine serum (FBS) and antibiotics (100 U/ml penicillin and 100 mg/ml streptomycin) at 37 °C in an atmosphere of 5% CO2. All cells tested negative for mycoplasma contamination, and this result was verified by short tandem repeat (STR) fingerprinting before use.

Northern blot
A total of 10 µg of the extracted RNA was subjected to formaldehyde denaturing gel electrophoresis and transferred to a nylon membrane. Subsequently, the blotted membrane was prehybridized at 50 °C with the DIG Easy Hyb buffer (#11796895001, Roche) for 1 h, followed by further incubation with a digoxigenin (DIG)-labeled *ZNF252P* probes at 50 °C overnight. The probe–target hybrids were detected by the DIG Luminescent Detection kit (#11363514910, Roche). The probe sequences are listed in Supplementary Table 2.

Rapid amplification of cDNA ends analysis (RACE)
The rapid amplification of cDNA ends (RACE) analysis was performed using a SMARTer RACE 5/3′ Kit (Clontech) according to the manufacturer's instructions. The sequences for the gene-specific PCR primers used for 5′ and 3′ RACE are presented in Supplementary Table 2.

Cell transfection
After the cells were plated in six-well plates, the small interfering RNA (siRNA) or ASO (antisense oligonucleotide) was transfected into cells using Lipofectamine (Invitrogen), including the corresponding controls. The sequences are provided in Supplementary Table 2. The *ZNF252P* sequence was subcloned into a pcDNA3.1 vector (Invitrogen). The pcDNA-*ZNF252P* vector was transfected into cells using the X-tremeGENE HP DNA transfection reagent (Roche). The experiments were independently replicated three times.

RNA extraction, DNA extraction and qRT-PCR analyses
Total RNA was extracted using TRIzol reagent according to the protocol (Invitrogen). For qRT-PCR assays, we used the Reverse Transcription Kit (Vazyme) to reverse transcribe RNA to cDNA. The qPCR assays were performed with SYBR Green (Vazyme). Results were normalized to the expression of *β-actin*. The DNA was isolated according to the DNA extraction procedure. *LINE1* (long interspersed element 1) was used as the genomic level internal control. The qRT-PCR and data collection were conducted using an ABI 7500 real-time PCR system (Applied Biosystems, USA). The primer sequence is provided in Supplementary Table 2.

Cell proliferation assays
Transfected cells were seeded in the 96-well plates, and the MTT kit (Sigma) was used to test the cell viability every 24 h. For the colony formation assay, transfected cells were seeded in the 6-well plates and maintained in proper media for 2 weeks. After being fixed with methanol and stained with 0.1% crystal violet for 15 min, the proliferation capacity was determined by measuring the colony area. For the EdU assay, we conducted the assays by using the EdU Cell Proliferation Assay Kit (RiboBio) according to the protocol.

Western blot assay
The cell protein lysates were separated by 10% sodium dodecyl sulfate-polyacrylamide gel electrophoresis (SDS-PAGE), and proteins were transferred to 0.22 µm PVDF membranes (Millipore) and incubated with specific antibodies. The autoradiograms were quantified by densitometry (Quantity One software; Bio-Rad). β-actin antibody (Proteintech, dilution ratio, 1:10000, 66009-1-Ig) was used as the control. Lamin B1(Dilution ratio, 1:5000, 12987-1-AP) was from Proteintech. C-Myc antibody (Dilution ratio, 1:1000, 18583S) was from Cell Signaling Technology. ILF3 antibody (Dilution ratio, 1:2000, ab131004), HNRNPK antibody (Dilution ratio, 1:2000, ab70492) were from Abcam. MYCL antibody (Dilution ratio, 1:1000, A16301), MLXIPL antibody (Dilution ratio, 1:1000, A7630) were from Abclonal. MXD4 antibody (Dilution ratio, 1:2000, PA5-40596) was from Invitrogen. All uncropped blots were included in the Source Data file.

Dual-luciferase reporter assays
Dual-luciferase reporter assays were performed via the Dual-Luciferase® Reporter Assay System Kit according to the manufacturer's protocol (Promega, USA). The cells were cotransfected with the constructed target luciferase vector and the Renilla luciferase plasmid. The luciferase activity of each sample was determined by normalizing the luminescence value of Renilla luciferase to that of the firefly luciferase.

Chromatin immunoprecipitation (ChIP) assays
The ChIP assays were performed by using the EZ-CHIP Kit according to the manufacturer's protocol (Cat.17-408, Millipore). The c-Myc antibody was obtained from Cell Signaling Technology (18583S), and the HNRNPK antibody was from Abcam (ab70492). The quantification of immunoprecipitated DNA was determined via qRT–PCR analysis. The ChIP data were calculated as a percentage relative to the input DNA

https://doi.org/10.1038/s41467-025-56879-7

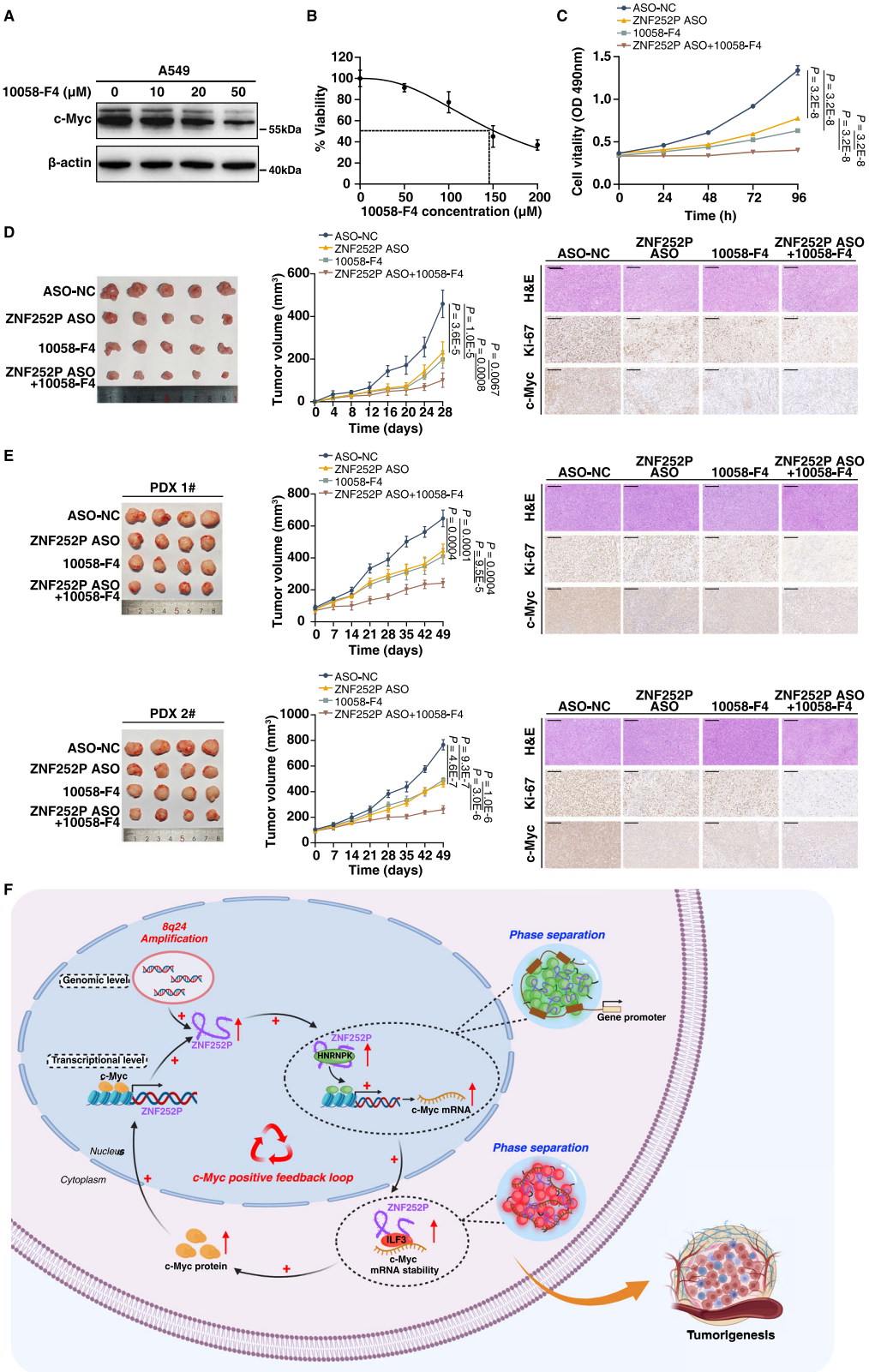

using the equation $2^{[\text{Input Ct- Target Ct}]} \times 100$ (%). The ChIP primers are listed in Supplementary Table 2.

Vitro transcription assays and RNA pulldown/mass spectrometry analysis

The indicated gene for the experiments were transcribed in vitro via a mMESSAGE mMACHINE T7 transcription kit according to the manufacturer's protocol (Cat.AM1344; Invitrogen). We used the Pierce RNA 3′ End Desthiobiotinylation Kit (Cat.20164, Thermo) to label the RNA with desthiobiotization, followed by RNA pull-down assays via the Pierce Magnetic RNA–protein Pull-Down Kit (Cat.20164, Thermo). Proteins obtained by RNA pulldown were used for Western blot or digested into peptides for mass spectrometry (MS) analysis. LC/MS-MS experiments were performed with a

Fig. 9 | The therapeutic effects of *ZNF252P*/*c-Myc* in tumorigenesis. A The immunoblotting assay detected c-Myc expression after treatment with the different concentrations of 10058-F4. Data are representatives of 3 independent experiments. **B** IC50 assay showed decreased cell viability as 10058-F4 concentration rose. Data are mean ± s.d.; $n = 3$ independent experiments. **C** MTT assay detected the effect of indicated treatments on cell proliferation. Data are mean ± s.d.; $n = 3$ independent experiments, one-way ANOVA with Dunnett's multiple comparisons test. **D** The cell xenograft model in nude mice showed the better tumor inhibition effect with the combination of 10058-F4 and *ZNF252P* ASO (intratumoral injection). Tumor sections were stained with antibodies against Ki-67 and c-Myc. Scale bar 200μm. Data are representatives or mean ± s.d.; $n = 5$ mice per group, one-way ANOVA with Dunnett's multiple comparisons test. **E** The combination of 10058-F4 and *ZNF252P* ASO reduced the tumor growth in PDX models (PDX 1# and PDX 2#). Tumor sections were stained with antibodies against Ki-67 and c-Myc. Scale bar 200μm. Data are representatives or mean ± s.d.; $n = 4$ mice per group, one-way ANOVA with Dunnett's multiple comparisons test. **F** The schematic model of *8q24*-driven *ZNF252P* in cancer. This diagram was created in BioRender. Zhang, E. (2025) https://BioRender.com/k34r796. Source data are provided as a Source data file.

QExactive Orbitrap mass spectrometer (Thermo Finnigan) equipped with a nanospray source.

RNA immunoprecipitation (RIP) assays
The RIP assays were performed via the Magna RIP™ RNA-Binding Protein Immunoprecipitation Kit according to the manufacturer's protocol (Cat.17-701, Millipore). The HNRNPK antibody (ab70492) and the ILF3 antibody (ab131004) were obtained from Abcam.

Crosslinking immunoprecipitation (CLIP)
The CLIP assay was performed according to the previously reported protocol[65]. Briefly, after UV crosslinking, cells were lysed and centrifuged to obtain supernatant, followed by digestion with RNase. Then, we utilized magnetic beads coated with the HNRNPK antibody (ab70492) and ILF3 antibody (ab131004) for immunoprecipitation of the RNA-protein complex (IgG as control). Then the complex was purified using protein gels and transferred to the nitrocellulose membrane. After that, the immunoprecipitated RNA was isolated for qRT-PCR analysis.

Subcellular fractionation
Separation of the nuclear and cytosolic fractions was performed using the PARIS Kit (Cat. AM1921, Invitrogen, CA, USA) according to the manufacturer's instructions.

RNA fluorescence in situ hybridization (FISH) and immunofluorescence (IF) microscopy assays
For RNA FISH, after being washed with PBS, the cells were fixed with 4% paraformaldehyde in PBS for 15 min. The cells were subsequently infiltrated with PBS containing 0.2% Triton X-100 and 5 mM vanadyl riboside complex on ice for 5 min, washed with PBS three times and rinsed once with SSC buffer. Hybridization was performed in a moist chamber at 37 °C for 16 h via Cy3-labeled *ZFN252P* or Cy5-labeled *c-Myc* mRNA probes according to the protocol for adherent cell lines. For colocalization assays, after RNA-FISH, the cells were washed for 5 min, twice in PBST, then once in 50% PBST and subjected to immunofluorescence for the target protein. Cells were stained overnight at 4°C with primary antibodies against HNRNPK antibody (ab70492, Abcam) or ILF3 antibody (PA5-115420, Invitrogen) at a dilution of 1:300 or 1:500 in blocking solution, followed by incubation with secondary antibodies (1:500 dilution) and DAPI (Invitrogen). The slides were subsequently analyzed via confocal fluorescence microscopy (LSM710, Zeiss).

Protein purification
The plasmids containing a GFP/mCherry tag were transformed into BL21 (DE3) *E. coli* cells for IPTG-induced protein expression[66]. Briefly, the cell pellets obtained from the Terrific Broth (TB) medium culture were further centrifuged to precipitate the cells. After the cell pellets were resuspended in the lysis buffer (50 mM Tris-HCl pH 7.5, 500 mM NaCl, 10 mM imidazole and 1 × protease inhibitors), sonication was used to lyse the cells. The supernatant was collected after centrifugation for further purification. The target protein was obtained through two-step purification via a Ni column and Superdex 200 columns (GE Healthcare), and the purified protein was stored in storage buffer at -80 °C after being flash-frozen in liquid nitrogen.

Plasmids and constructs
We synthesized *ZNF252P* cDNA and cloned it into pcDNA3.1. The fragments of *ZNF252P* for RNA pull down assays were used as a template to generate constructs with deletions. Using the synthesized GFP-HNRNPK or mCherry-ILF3 constructs as the templates, we generated the following plasmids. Mutant GFP-HNRNPK or mCherry–ILF3 containing mutations and various truncations in the HNRNPK or ILF3 molecule were generated by PCR and similarly cloned into the above vectors. The chimeric GFP-HNRNPK molecules containing HNRNPK-IDR (amino acids 247-438), HNRNPK-IDR^{DEL}, HNRNPK-IDR^{MUT} were generated by PCR based on the GFP-HNRNPK. The chimeric mCherry-ILF3 molecules containing ILF3-IDR (amino acids 342-898), ILF3-IDR^{DEL}, ILF3-IDR^{MUT} were generated by PCR based on the mCherry–ILF3. For IDR^{MUT}, the IDR of HNRNPK and ILF3 contains compositional bias for glycine. We mutated all the glycine residues to threonine, creating the IDR MUT type. All the PCR products were verified by DNA sequencing.

Droplet assays
The purified recombinant GFP-HNRNPK or mCherry-ILF3 proteins were subjected to concentration and dissolution to reach the indicated protein concentration. Then the droplet formation buffer (50 mM Tris-HCl pH 7.5, 10% glycerol, 1 mM DTT) was supplemented with the indicated protein, along with the specified final concentration of salt (NaCl) and 10% PEG-8000 (crowding agent)[67]. For the experiment of droplet assays, the protein or RNA-protein solution used to form droplets was loaded into a self-made chamber, which was composed of a coverslip and a glass slide fixed on it through two parallel double-sided tapes, and imaging of the slides was performed via microscope using a 40 × objective (LSM710, Zeiss). For droplet assays in the cell, A549 cells expressing GFP-HNRNPK or mCherry-ILF3 were transfected with the corresponding experimental treatment. After trypsin digestion and collection, the cells were washed with TBS. Then the cells were re-suspended in a hypotonic solution (10 mM HEPES pH 7.9, 1.5 mM MgCl2, 10 mM KCl, 1 mM DTT, protease inhibitor) and incubated for 5 min on ice. Following the subsequent addition of 0.1% NP-40, cells were incubated for an additional 5 min on ice. After centrifuging the cells at 376 × g for 10 min, the supernatant was retrieved and subjected to incubation for 15 min on ice. Following centrifugation at 21130 × g at 4 °C, the supernatant was precipitated by ammonium sulfate and the protein was acquired through dialysis[68]. Subsequently, the proteins in the droplet buffer were loaded onto a coverslip-coated slide and imaged via confocal fluorescence microscopy using a 40 × objective (LSM710, Zeiss). The droplet formation was followed over time via collecting a series of images in both the bright field and fluorescent channels.

Live cell imaging
In brief, the transfected A549 cells were seeded in confocal dishes. After 48 h, they were washed with PBS and fixed with 4% paraformaldehyde for 10 min. Then, they were washed and kept with PBS

and imaged by a confocal microscope with × 63 oil-immersion lens (Zeiss)[52].

Fluorescence recovery after photobleaching (FRAP) assays
FRAP assays were carried out via a confocal fluorescence microscope furnished with oil-immersed objective lens (Zeiss). The droplets were individually bleached with laser pulses. Briefly, the circular region of interest (ROI) was bleached using laser power (100%) and time-lapse images were acquired[69]. For the target spot, the bleaching conditions entail the utilization of the maximum laser intensity and pixel dwell time that correspond to the total bleaching time for bleaching[70]. During the prescribed time, the recovery following photobleaching was documented and analyzed.

Transcriptome sequencing analysis
The total RNA of A549 cells transfected with *ZNF252P* knockdown and the control cells were extracted. After measuring the concentration, the quality of RNA was assessed by Agilent2200. The sequencing library of each RNA sample was prepared using the TruSeq Stranded mRNA Library Prep Kit (Illumina). The sequencing data was presented in Supplementary Data 3.

Gene Set Enrichment Analysis (GSEA) analysis
The differentially expressed genes after *ZNF252P* knockdown were used for GSEA analyses against the Molecular Signatures Database (MSigDB) Hallmark gene sets and KEGG gene sets (http://software.broadinstitute.org/gsea/msigdb). Then the GSEA analysis was performed using GSEA software 4.0.3 by the Broad Institute (http://software.broadinstitute.org).

DNA probe production
The probe DNA fragment was amplified from tumor DNA via PCR from the specific region of the c-Myc promoter. Amplification of the genomic DNA templates was performed via KOD FX Neo polymerase (TOYOBO). The Cy5-labeled probes were purified via a gel extraction kit (Tiangen). The wild-type and HNRNPK motif mutation c-Myc promoter DNA sequences are provided in Supplementary Table 2.

dCas9-SunTag c-Myc promoter visualization assays
The assay for c-Myc promoter visualization was performed as previously described[44]. Briefly, the sgRNAs around the c-Myc promoter were cloned into a PUC19 backbone via the Golden Gate reaction. pTETON-dCas9-24*GCN4, pTETon-scFv-GCN4-sfGFP and sgRNA were cotransfected into A549 cells. Then the cells were prepared for immunofluorescence staining. The primary antibodies were anti-HNRNPK (Abcam, ab70492). The secondary antibodies were anti-rabbit Alexa Fluor 594 (Invitrogen, A32754). SIM analysis was performed via superresolution microscope (ZEISS). The sequences of the sgRNAs are provided in Supplementary Table 2.

RNA stability assays
The transfected cells were treated with actinomycin D (10 μg/ml, Selleckchem) and cultured for the indicated time. After the RNA was extracted, qRT–PCR was used to analyze the remaining mRNA. 18S rRNA was used to normalize gene expression.

Animal experiments
Five-week-old male BALB/c nude mice were housed under specific pathogen free (SPF) conditions. Mice were housed under controlled conditions (24–26 °C, 40–70% humidity) with a 12 h light/dark cycle. Sterile food and water were provided throughout the housing period. To generate cell-derived xenografts, the transfected cells were xenografted into BALB/c male nude mice. To generate the patient-derived xenograft (PDX) model, tumor samples were cut into appropriate small fragments and inoculated into the subcutaneous space of 5 week-old male NCG mice. When the tumor volume reached an appropriate size, the mice were intratumorally administered with the in vivo-optimized ASO or control (5 nmol per injection, RiboBio) every 4 days. To explore the efficiency of 10058-F4, the mice were injected daily with 30 mg/kg 10058-F4 (MedChemExpress, MCE) when the tumors were palpable. The tumor volume and weight were measured at regular intervals. The tumor volume was calculated as follows: volume = 0.5 × length × width^2. After the inoculation of the xenografts, the size of the transplanted tumor was monitored daily. The mice were euthanized when exhibiting the degradation of the general condition, performance status, or 20% loss of weight. All animals were euthanized according to the IACUC guidelines. Then the tumors were weighed and used for further pathological analysis. The maximal tumor burden permitted by the IACUC of Nanjing Medical University is 2000 mm^3. In this study, the tumor burden was not exceeded at any point.

Statistics and reproducibility
The data were analyzed using R (v3.6.1) software, GraphPad Prism 8.3.0, and ImageJ software 1.8.0. The data were represented as the mean ± standard deviation. The difference between two groups was evaluated by two-tailed Student's *t*-test, whereas the difference among multiple groups was evaluated by one-way ANONA. Corresponding figure legends indicate sample sizes and significance levels. A value of $P < 0.05$ was considered statistically significant.

Reporting summary
Further information on research design is available in the Nature Portfolio Reporting Summary linked to this article.

Data availability
The RNA-seq data has been deposited in NCBI Gene Expression Omnibus and are accessible through GEO accession number GSE271524. The mass spectrometry proteomics data has been deposited to the ProteomeXchange Consortium via the PRIDE partner repository with the dataset identifier PXD053695. Source data are provided with this paper.

References

1. Hanahan, D. Hallmarks of cancer: new dimensions. *Cancer Discov.* **12**, 31–46 (2022).
2. Tanaka, H. & Watanabe, T. Mechanisms underlying recurrent genomic amplification in human cancers. *Trends Cancer* **6**, 462–477 (2020).
3. Zhao, M. & Zhao, Z. Concordance of copy number loss and down-regulation of tumor suppressor genes: a pan-cancer study. *BMC Genomics* **17**, 532 (2016).
4. Recondo, G., Che, J., Janne, P. A. & Awad, M. M. Targeting MET dysregulation in cancer. *Cancer Discov.* **10**, 922–934 (2020).
5. Tu, R., Chen, Z., Bao, Q., Liu, H. & Qing, G. Crosstalk between oncogenic MYC and noncoding RNAs in cancer. *Semin Cancer Biol.* **75**, 62–71 (2021).
6. Jehan, Z. et al. Frequent PIK3CA gene amplification and its clinical significance in colorectal cancer. *J. Pathol.* **219**, 337–46 (2009).
7. Wang, X. et al. Recurrent amplification of MYC and TNFRSF11B in 8q24 is associated with poor survival in patients with gastric cancer. *Gastric Cancer* **19**, 116–27 (2016).
8. Guan, Y. et al. Amplification of PVT1 contributes to the pathophysiology of ovarian and breast cancer. *Clin. Cancer Res.* **13**, 5745–55 (2007).
9. Pouryazdanparast, P. et al. The role of 8q24 copy number gains and c-Myc expression in amelanotic cutaneous melanoma. *Mod. Pathol.* **25**, 1221–6 (2012).
10. Riquelme, E. et al. Frequent coamplification and cooperation between C-MYC and PVT1 oncogenes promote malignant pleural mesothelioma. *J. Thorac. Oncol.* **9**, 998–1007 (2014).

11. Statello, L., Guo, C. J., Chen, L. L. & Huarte, M. Gene regulation by long non-coding RNAs and its biological functions. *Nat. Rev. Mol. Cell Biol.* **22**, 96–118 (2021).
12. Zhu, Q. et al. MNX1-AS1 promotes phase separation of IGF2BP1 to drive c-Myc-mediated cell-cycle progression and proliferation in lung cancer. *Cancer Res.* **82**, 4340–4358 (2022).
13. Zhang, E. et al. A novel long noncoding RNA HOXC-AS3 mediates tumorigenesis of gastric cancer by binding to YBX1. *Genome Biol.* **19**, 154 (2018).
14. Zhang, E. et al. H3K27 acetylation activated-long non-coding RNA CCAT1 affects cell proliferation and migration by regulating SPRY4 and HOXB13 expression in esophageal squamous cell carcinoma. *Nucleic Acids Res.* **45**, 3086–3101 (2017).
15. Lu, X. et al. Copy number amplification and SP1-activated lncRNA MELTF-AS1 regulates tumorigenesis by driving phase separation of YBX1 to activate ANXA8 in non-small cell lung cancer. *Oncogene* **41**, 3222–3238 (2022).
16. Tseng, Y. Y. et al. PVT1 dependence in cancer with MYC copy-number increase. *Nature* **512**, 82–6 (2014).
17. Hu, X. et al. A functional genomic approach identifies FAL1 as an oncogenic long noncoding RNA that associates with BMI1 and represses p21 expression in cancer. *Cancer Cell* **26**, 344–357 (2014).
18. Banani, S. F., Lee, H. O., Hyman, A. A. & Rosen, M. K. Biomolecular condensates: organizers of cellular biochemistry. *Nat. Rev. Mol. Cell Biol.* **18**, 285–298 (2017).
19. Alberti, S., Gladfelter, A. & Mittag, T. Considerations and challenges in studying liquid-liquid phase separation and biomolecular condensates. *Cell* **176**, 419–434 (2019).
20. Chakravarty, A. K. et al. Biomolecular condensation: a new phase in cancer research. *Cancer Discov.* **12**, 2031–2043 (2022).
21. Lin, C. C. et al. Receptor tyrosine kinases regulate signal transduction through a liquid-liquid phase separated state. *Mol. Cell* **82**, 1089–1106.e12 (2022).
22. Shao, W. et al. Phase separation of RNA-binding protein promotes polymerase binding and transcription. *Nat. Chem. Biol.* **18**, 70–80 (2022).
23. Boija, A., Klein, I. A. & Young, R. A. Biomolecular condensates and cancer. *Cancer Cell* **39**, 174–192 (2021).
24. Fu, Y. & Zhuang, X. m(6)A-binding YTHDF proteins promote stress granule formation. *Nat. Chem. Biol.* **16**, 955–963 (2020).
25. Lin, Y., Protter, D. S., Rosen, M. K. & Parker, R. Formation and maturation of phase-separated liquid droplets by RNA-binding proteins. *Mol. Cell* **60**, 208–19 (2015).
26. Langdon, E. M. & Gladfelter, A. S. A new lens for RNA localization: liquid-liquid phase separation. *Annu Rev. Microbiol* **72**, 255–271 (2018).
27. Fay, M. M. & Anderson, P. J. The role of RNA in biological phase separations. *J. Mol. Biol.* **430**, 4685–4701 (2018).
28. Elguindy, M. M. & Mendell, J. T. NORAD-induced pumilio phase separation is required for genome stability. *Nature* **595**, 303–308 (2021).
29. Wu, Y. et al. Disrupting the phase separation of KAT8-IRF1 diminishes PD-L1 expression and promotes antitumor immunity. *Nat. Cancer* **4**, 382–400 (2023).
30. Sheu-Gruttadauria, J. & MacRae, I. J. Phase transitions in the assembly and function of human miRISC. *Cell* **173**, 946–957.e16 (2018).
31. Li, R., Wang, X., Zhu, C. & Wang, K. lncRNA PVT1: a novel oncogene in multiple cancers. *Cell Mol. Biol. Lett.* **27**, 84 (2022).
32. Qin, H. D. et al. Genomic characterization of esophageal squamous cell carcinoma reveals critical genes underlying tumorigenesis and poor prognosis. *Am. J. Hum. Genet* **98**, 709–27 (2016).
33. Wang, Y. et al. High cancer susceptibility candidate 8 expression is associated with poor prognosis of pancreatic adenocarcinoma: validated analysis based on four cancer databases. *Front Cell Dev. Biol.* **8**, 392 (2020).
34. Shaath, H. et al. Long non-coding RNA and RNA-binding protein interactions in cancer: experimental and machine learning approaches. *Semin Cancer Biol.* **86**, 325–345 (2022).
35. Chen, Y. et al. HNRNPK is essential for embryonic limb bud development as a transcription activator and a collaborator of insulator protein Ctcf. *Cell Death Differ.* **30**, 2293–2308 (2023).
36. Liu, Y. et al. Upregulation of ERp57 promotes clear cell renal cell carcinoma progression by initiating a STAT3/ILF3 feedback loop. *J. Exp. Clin. Cancer Res.* **38**, 439 (2019).
37. Patiyal, S., Dhall, A., Bajaj, K., Sahu, H. & Raghava, G. P. S. Prediction of RNA-interacting residues in a protein using CNN and evolutionary profile. *Brief. Bioinform.* **24**, bbac538 (2023).
38. Hirose, T., Ninomiya, K., Nakagawa, S. & Yamazaki, T. A guide to membraneless organelles and their various roles in gene regulation. *Nat. Rev. Mol. Cell Biol.* **24**, 288–304 (2023).
39. Garner, E., Romero, P., Dunker, A. K., Brown, C. & Obradovic, Z. Predicting binding regions within disordered proteins. *Genome Inf. Ser. Workshop Genome Inf.* **10**, 41–50 (1999).
40. Dunker, A. K. et al. Intrinsically disordered protein. *J. Mol. Graph Model* **19**, 26–59 (2001).
41. Langdon, E. M. et al. mRNA structure determines specificity of a polyQ-driven phase separation. *Science* **360**, 922–927 (2018).
42. Garcia-Jove Navarro, M. et al. RNA is a critical element for the sizing and the composition of phase-separated RNA-protein condensates. *Nat. Commun.* **10**, 3230 (2019).
43. Grandori, C., Cowley, S. M., James, L. P. & Eisenman, R. N. The Myc/Max/Mad network and the transcriptional control of cell behavior. *Annu Rev. Cell Dev. Biol.* **16**, 653–99 (2000).
44. Shao, S. et al. Multiplexed sgRNA expression allows versatile single nonrepetitive DNA labeling and endogenous gene regulation. *ACS Synth. Biol.* **7**, 176–186 (2018).
45. Yu, X. X. et al. Antisense oligonucleotide reduction of DGAT2 expression improves hepatic steatosis and hyperlipidemia in obese mice. *Hepatology* **42**, 362–71 (2005).
46. Fichtner, I. et al. Establishment of patient-derived non-small cell lung cancer xenografts as models for the identification of predictive biomarkers. *Clin. Cancer Res.* **14**, 6456–68 (2008).
47. Tsang, S. V. et al. LncRNA PVT-1 promotes osteosarcoma cancer stem-like properties through direct interaction with TRIM28 and TSC2 ubiquitination. *Oncogene* **41**, 5373–5384 (2022).
48. Kim, Y. H. et al. Combined microarray analysis of small cell lung cancer reveals altered apoptotic balance and distinct expression signatures of MYC family gene amplification. *Oncogene* **25**, 130–8 (2006).
49. Hayashi, H. et al. The OCT4 pseudogene POU5F1B is amplified and promotes an aggressive phenotype in gastric cancer. *Oncogene* **34**, 199–208 (2015).
50. Savelyeva, L. & Schwab, M. Amplification of oncogenes revisited: from expression profiling to clinical application. *Cancer Lett.* **167**, 115–23 (2001).
51. Dang, C. V. MYC on the path to cancer. *Cell* **149**, 22–35 (2012).
52. Li, R. H. et al. A phosphatidic acid-binding lncRNA SNHG9 facilitates LATS1 liquid-liquid phase separation to promote oncogenic YAP signaling. *Cell Res.* **31**, 1088–1105 (2021).
53. Wang, R. et al. LncRNA GIRGL drives CAPRIN1-mediated phase separation to suppress glutaminase-1 translation under glutamine deprivation. *Sci. Adv.* **7**, eabe5708 (2021).
54. Cai, D. et al. Phase separation of YAP reorganizes genome topology for long-term YAP target gene expression. *Nat. Cell Biol.* **21**, 1578–1589 (2019).
55. Yu, M. et al. Interferon-gamma induces tumor resistance to anti-PD-1 immunotherapy by promoting YAP phase separation. *Mol. Cell* **81**, 1216–1230.e9 (2021).

56. Sahin, C. et al. Mass spectrometry of RNA-binding proteins during liquid-liquid phase separation reveals distinct assembly mechanisms and droplet architectures. *J. Am. Chem. Soc.* **145**, 10659–10668 (2023).
57. Molliex, A. et al. Phase separation by low complexity domains promotes stress granule assembly and drives pathological fibrillization. *Cell* **163**, 123–33 (2015).
58. Tomonaga, T. & Levens, D. Activating transcription from single stranded DNA. *Proc. Natl Acad. Sci. USA* **93**, 5830–5 (1996).
59. Zanconato, F., Cordenonsi, M. & Piccolo, S. YAP/TAZ at the roots of cancer. *Cancer Cell* **29**, 783–803 (2016).
60. Zheng, Y. & Pan, D. The hippo signaling pathway in development and disease. *Dev. Cell* **50**, 264–282 (2019).
61. Ren, D. et al. SGLT2 promotes pancreatic cancer progression by activating the hippo signaling pathway via the HNRNPK-YAP1 axis. *Cancer Lett.* **519**, 277–288 (2021).
62. Xia, A. et al. The cancer-testis lncRNA lnc-CTHCC promotes hepatocellular carcinogenesis by binding hnRNP K and activating YAP1 transcription. *Nat. Cancer* **3**, 203–218 (2022).
63. Goldman, M. J. et al. Visualizing and interpreting cancer genomics data via the Xena platform. *Nat. Biotechnol.* **38**, 675–678 (2020).
64. Teng, L. et al. The pan-cancer lncRNA PLANE regulates an alternative splicing program to promote cancer pathogenesis. *Nat. Commun.* **12**, 3734 (2021).
65. Van Nostrand, E. L. et al. Robust transcriptome-wide discovery of RNA-binding protein binding sites with enhanced CLIP (eCLIP). *Nat. Methods* **13**, 508–14 (2016).
66. Wang, C. et al. Stress induces dynamic, cytotoxicity-antagonizing TDP-43 nuclear bodies via paraspeckle LncRNA NEAT1-mediated liquid-liquid phase separation. *Mol. Cell* **79**, 443–458.e7 (2020).
67. Boija, A. et al. Transcription factors activate genes through the phase-separation capacity of their activation domains. *Cell* **175**, 1842–1855.e16 (2018).
68. Pessina, F. et al. Functional transcription promoters at DNA double-strand breaks mediate RNA-driven phase separation of damage-response factors. *Nat. Cell Biol.* **21**, 1286–1299 (2019).
69. Zhu, G. et al. Phase separation of disease-associated SHP2 mutants underlies MAPK hyperactivation. *Cell* **183**, 490–502.e18 (2020).
70. Wang, L. et al. Histone modifications regulate chromatin compartmentalization by contributing to a phase separation mechanism. *Mol. Cell* **76**, 646–659.e6 (2019).

Acknowledgements

This work was supported by National Natural Science Foundation of China [82472672 and 82172992 to EBZ, 82172982 to DDY, 82273171 to LH, 82403029 to CZ, 82103133 to XYL] and Jiangsu Province Science and Technology Project [BK20211253 to EBZ, BK20231156 to LH and BK20210973 to XYL]. This work was also supported by Jiangsu Province Excellent Postdoctoral Program [2023ZB419 to CZ] and China Postdoctoral Science Foundation [2023M740371 to CZ].

Author contributions

Conception and design: EBZ. Development of methodology: TYQ, CZ and XZH. Acquisition of data: TYQ, CZ, XYL and JLD. Analysis of data: TYQ and CZ. Writing, review, and revision of manuscript: TYQ and EBZ. Administrative, technical, or material support: WL, LH, DDY and EBZ.

Competing interests

The authors declare no competing interests.

Additional information

Supplementary information The online version contains supplementary material available at https://doi.org/10.1038/s41467-025-56879-7.

Correspondence and requests for materials should be addressed to Liang Han, Dandan Yin or Erbao Zhang.

Peer review information *Nature Communications* thanks Marie-Eve Beaulieu, and the other, anonymous, reviewer(s) for their contribution to the peer review of this work. A peer review file is available.

Reprints and permissions information is available at http://www.nature.com/reprints

Publisher's note Springer Nature remains neutral with regard to jurisdictional claims in published maps and institutional affiliations.

Open Access This article is licensed under a Creative Commons Attribution-NonCommercial-NoDerivatives 4.0 International License, which permits any non-commercial use, sharing, distribution and reproduction in any medium or format, as long as you give appropriate credit to the original author(s) and the source, provide a link to the Creative Commons licence, and indicate if you modified the licensed material. You do not have permission under this licence to share adapted material derived from this article or parts of it. The images or other third party material in this article are included in the article's Creative Commons licence, unless indicated otherwise in a credit line to the material. If material is not included in the article's Creative Commons licence and your intended use is not permitted by statutory regulation or exceeds the permitted use, you will need to obtain permission directly from the copyright holder. To view a copy of this licence, visit http://creativecommons.org/licenses/by-nc-nd/4.0/.

© The Author(s) 2025